Chapter 7

Observation of magnetic transitions and Kondo effect in the electrical resistivity of Mn_3GaN antiperovskite thin film

In this chapter, we demonstrate the first signature of a single impurity Kondo effect and a series of magnetic transitions in the temperature-dependent resistivity data of the Mn_3GaN compound. Furthermore, Hall data reveals the existence of AHE, which is likely attributed to spin canting from non-collinear antiferromagnetic ordering with Γ^{5g} magnetic symmetry due to the coexisting phase of ferrimagnetic ordering.

7.1 Introduction

Antiperovskites with a general formula X_3BA (X = transition metals such as Mn, Co, Fe, Ni; B = a transition or main group element such as Ga, Al, In, Zn, Sn; and A = C, N, and B) constitute an important class of materials with potential for a diverse range of technologically useful functional and multifunctional applications linked with phenomena like geometrically frustrated magnetism [1, 2, 3, 4], giant magnetoresitivity [5], magnetostriction [6, 8], magnetocaloricity [7, 9], superionic conductivity [10, 11, 12], superconductivity [13, 14], meta-thermal expansivity [15, 16, 17, 18], electrocatalysis [19], luminescence [20, 21], to name a few. The structure of these antiperovskites offers enormous flexibility in accommodating various chemical substitutions at the three sites and, thereby, the scope for improving the functional behavior of these materials. Among these antiperovskite compounds, the metallic and (antiferro-) magnetic antiperovskites with the chemical formula Mn_3BA, where B can be Ni, Ga, Sn, Cu, etc. while A can be C, N, B, have attracted a lot of attention in recent years due to their large negative thermal expansion [22, 23, 24, 25], large magnetovolume effect [26], giant barocaloric effect [27], large anomalous Hall effect [28, 29, 30, 31], anomalous Nernst effect [32, 33] and electrical switching of spin-orbit torque [34, 35]. Here we present the first evidence for another exotic phenomenon, namely the under-screened single impurity Kondo effect with localized spin S = 3/2 in a geometrically frustrated antiferromagnetic compound Mn_3GaN, belonging to the family of antiperovskites. We believe that our findings open new possibilities for exploring the fascinating electronic correlation effects in the family of geometrically frustrated antiferromagnetic X_3BA type compounds containing other possible elements at the X (such as Co, Fe, Ni), A (such as C, O) and, B (such as Ge, Cu, Zn) sites with different concentration of anti-site disorder.

The study of strongly correlated systems has been a time-honored problem in solid state and materials sciences [36]. The Kondo effect is one such interesting phenomenon, where normal metallic hosts like Au, Ag, Cu, Zn, and Mg containing a very small concentration of magnetic impurities like Mn, Cr, Fe, Mo, Re, and Os were found to exhibit an anomalous logarithmic upturn in resistivity at low temperatures [37, 38, 39, 40, 41]. This was subsequently explained in terms of antiferromagnetic exchange coupling between the delocalized conduction electrons and localized spins associated with the magnetic impurity atoms [38, 39]. When the concentration of the magnetic impurity is sufficiently large, another resistivity minimum may appear above or below the Kondo minimum temperature depending on whether the RKKY interaction between the spins is stronger or weaker than the Kondo coupling [42, 43, 44, 45, 46]. Since the original discovery of the Kondo minimum in the temperature dependence of resistivity in dilute systems, it has been reported in a diverse range of materials like graphene [47] and indium tin oxide (ITO) nanowires [48], quantum dots based on Ga-Al-As interfaces [49] etc. without any doping with a magnetic element. The local magnetic spins in such systems are mostly due to the presence of defects/vacancies. For example, defects in graphene create an imbalance between its sublattices and result in the appearance of π-states with energy close to the Dirac point. As long as these states are singly occupied due to coulomb repulsion, they give rise to the magnetic moment [50]. In ITO nanowires, the oxygen vacancy in the vicinity of Sn sites acts as a magnetic impurity [48].

The Kondo effect has been extensively investigated in the heavy fermion Ce, Yb, U based intermetallics and compounds where the single-ion Kondo exchange interaction involving hybridization of almost localized 4f/5f moments with the itinerant electrons leads to the formation of a dense Kondo lattice or Kondo insulators with a finite band gap [51]. The on-site Kondo interaction in these systems competes with the inter-site long-range RKKY exchange interactions mediated by the itinerant Landau quasiparticles leading to long-range ordered magnetic states [45, 52, 53, 54, 55, 56]. In some of these compounds, non-thermal variables, like pressure, magnetic field, and composition, have been used to drive the system towards the quantum critical state with exotic properties [55, 57, 58, 59]. In most of these heavy fermion systems, the long-range ordered anti-ferromagnetic (LRO AFM) or ferromagnetic (FM) phase results in a temperature lower than the Kondo minimum temperature [60]. Recently single isolated impurity Kondo minimum and Kondo coherence, leading to the opening of a gap characteristic of a Kondo insulator, have been reported in a geometrically frustrated antiferromagnetic Weyl semimetal $Mn_{3+x}Sn_{1-x}$ films for x<0.40 and x>0.40, respectively [64]. It is interesting to note that the isolated impurity Kondo effect and coherence among them in $Mn_{3+x}Sn_{1-x}$ is not because of the magnetic spins taking part in the LRO AFM transition but is essentially due to anti-site disorder involving the 3d manganese (Mn) atoms occupying the Sn lattice sites in the crystal structure in marked contrast with the heavy fermion systems.

Motivated by this observation, we have explored the low-temperature resistivity behavior of Mn_3GaN thin films showing semiconducting-like behavior below ∼6 K, as intermixing of Mn and Ga (i.e., anti-site Mn/Ga disorder) has been reported in this compound [61, 62]. In similar Mn-based antiperovskite Mn_3SnN compound, the anomalous Hall effect (AHE) has been observed due to the weak magnetic moment induced by spin canting from Γ^{5g} antiferromagnetic spin configuration, as a result of the large displacement of the magnetic manganese atoms away from high-symmetry positions [63]. The angle of rotation of spin from the Γ^{5g} spin configuration exhibits variation with temperature and consequently, affect the AHE. Similar atomic displacement has also been expected in the Mn_3GaN compound [63]. Such an atomic disorder not only lowers the paramagnetic to LRO geometrically frustrated AFM transition temperature T_N ∼290 K of the stoichiometric compound but also leads to another magnetic transition below the T_N with systematic composition (x) dependence for $Mn_{4-x}Ga_xN$ [62]. This observation opens the possibility of observing isolated impurity Kondo effect and the AHE due to a very small fraction of Mn spins occupying the Ga lattice sites even in the so-called "stoichiometric" thin films of Mn_3GaN. That this indeed is the case has been confirmed in the present work using zero field and field dependent resistivity data, which reveal a resistivity minimum around 6 K with a logarithmic upturn and negative magnetoresistance. A detailed analysis of the resistivity data further shows that this resistivity minimum is due to an under-screened Kondo effect. Our observation opens the possibility of discovering dense Kondo insulator behavior in Mn_3GaN type compounds with antiperovskite structure as a function of the anti-site disorder similar to that reported in the AFM Weyl semimetals like $Mn_{3+x}Sn_{1-x}$ but different from the way it appears in the heavy fermion systems [51, 54, 65]. In high-temperature region, the analysis of the resistivity versus temperature data in terms of the Bloch-Gruneisen model reveals signatures of the paramagnetic (PM) to the AFM Γ^{5g} as well as the Γ^{5g} to the ferrimagnetic M-1 transitions reported recently in a neutron diffraction study [66] with different Debye temperatures for the two phases highlighting the complex interplay of electronic, lattice and spin degrees of freedom in Mn_3GaN. Besides a series of transitions in resistivity data, the Hall data reflects the presence of AHE, which might be related to a small finite rotation from the Γ^{5g} spin configuration.

7.2 Results and discussion

7.2.1 Methods

The thin film system with 150 nm thickness of Mn3GaN compound was deposited on a single crystal semiconducting Si (100) substrate using direct current magnetron sputtering (dcMS) technique with substrate temperature 350°C. A 2-inch-high purity (99.995%) MnGa target and 3-inch-high purity (99.995%) Mn were sputtered using a total of 50 standard cubic centimeters per minute (sccm) having a mixture of 45 sccm Ar (99.9995% purity) and 5 sccm, N_2 (99.999% purity) gases. The base pressure of 1.2×10^{-7} Torr or lower was achieved before deposition. The working pressure was about 2.4 mTorr due to the flow of process gases. After deposition, the x-ray diffraction (XRD) data was collected using a Rigaku X-ray diffractometer (wavelength $\sim$1.54 Å) to extract information about the crystal structure. In the deposition process, X-ray reflectivity was measured using a similar X-ray source (Bruker D8 Discover) to measure the film thickness. The thin film was subsequently examined using energy dispersive x-ray analysis (EDX), field emission scanning electron microscopy (FESEM), x-ray photoelectron spectroscopy (XPS), and X-ray absorption near edge spectroscopy (XANES) to confirm the phase formation and elemental composition. The composition of the samples is analyzed using EDX and XPS (K-Alpha from Thermo-scientific with monochromatized Al anode X-ray source). Back-scattered electron (BSE) image taken from SEM to confirm the uniform growth of the deposited film. XANES measurements at Mn L-edge and N K-edge were performed in total electron yield mode at soft x-ray absorption beamline (BL01) of Indus-2 synchrotron radiation source at RRCAT, Indore, India. The direct current (DC) magnetization measurements were performed on a Physical Property Measurement System (PPMS) of Quantum design (QD). Transport measurements were carried out using the alternating current transport (ACT) option of 9 T PPMS of QD. Resistivity and magnetoresistance measurements were performed by the four-probe method. To remove the transverse resistivity contribution in the M.R. data due to voltage probe misalignment, we have symmetrized the M.R. data by using the formula $\rho_{xx} = [\rho_{xx}(+H) + \rho_{xx}(-H)]/2$, where ρ_{xx} is the longitudinal resistivity.

7.2.2 XRD measurement

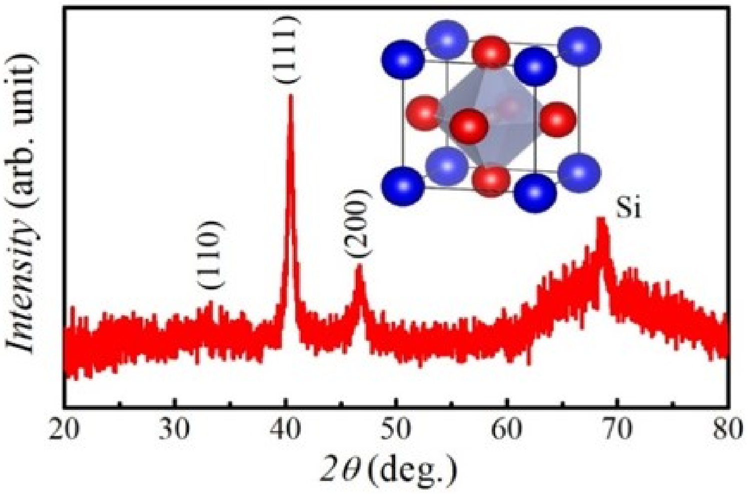

Figure 7.1: x-ray diffraction data at room temperature of thin film Mn_3GaN compound. Inset shows the crystal structure of the Mn_3GaN compound. The blue, red, and orange spheres represent the Ga, Mn, and N atoms, respectively

The XRD data [Fig. 7.1] of the thin film is collected at room temperature to confirm the phase formation. The different families of Bragg peaks in the XRD pattern reflect that the deposited thin film is polycrystalline and confirms the cubic antiperovskite phase formation in the space group Pm-3m with a lattice parameter a_{film} $\sim$3.89 Å, comparable to the value reported in the literature [67, 68]. The presence of different families of Bragg peaks in the XRD pattern reflects that the deposited thin film has nearly randomly oriented grains. Taking the lattice parameter of the Si substrate (a_{sub}) as 5.43 Å, the estimated lattice mismatch $[\frac{a_{\text{sub}}-a_{\text{film}}}{a_{\text{sub}}} \times 100\%]$ turns out to be around 28%, which is high enough to promote any textured growth. The absence of any detectable secondary phase peak in the XRD pattern reveals the phase-pure nature of the films.

7.2.3 BSE and EDX analysis

The BSE image [Fig. 7.2 (a)] shows uniform coverage of the film on the substrate, which confirms the homogeneous growth of thin film on the Si substrate. The EDX data [Fig. 7.2 (b)] collected by selecting different regions of the film confirms the average compositional ratio of Mn and Ga is 3:1. We performed XPS and XANES measurements to confirm nitrogen, as a light element is not reliably detectable by the EDX technique.

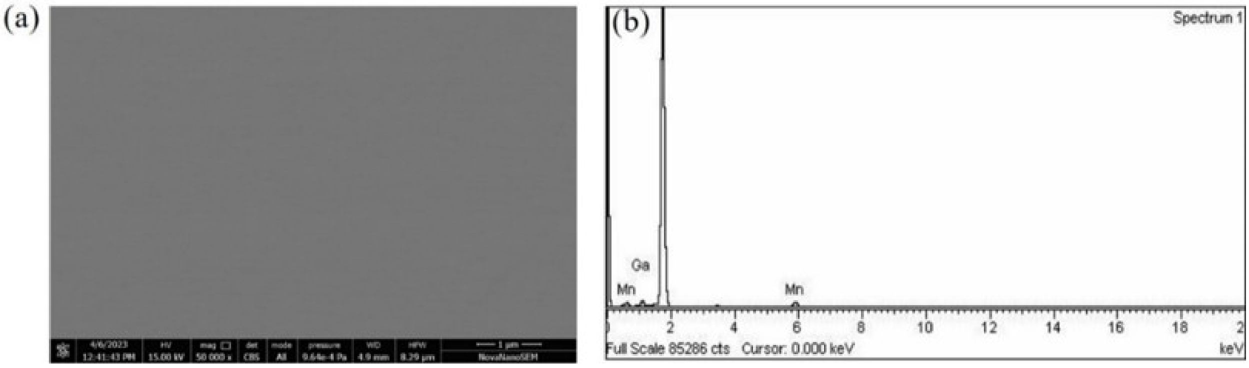

Figure 7.2: (a) BSE image of the Mn3GaN thin film. (b) EDX data represents Mn and Ga.

7.2.4 XPS analysis

The wide-range XPS spectra recorded for synthesized Mn_3GaN film reflect the characteristic photoemission peak of Mn, Ga, and N, confirming the presence of N along with the Mn and Ga in the grown Mn_3GaN film. The Mn (2p), Ga (2p), and N (1s) XPS spectra in higher resolution are shown in Fig. 7.3 (a-c). Fig. 7.3 (a) reflects the deconvoluted XPS spectra of Mn (2p) after linear background subtraction. Two peaks at binding energy (BE), 641.5 eV and 653.2 eV, indicate the Mn $2p_{3/2}$) and Mn $2p_{1/2}$ energy levels, respectively. There is a satellite peak centered at BE 647 eV. It has been reported that the peaks centered at BE 641.5 eV and 653.2 eV are assigned to Mn^{+2} ions, and the satellite peak centered at BE 647 eV is also a typical feature of Mn^{+2} ions [114]. As shown in Fig. 7.3 (b), the deconvoluted peaks of Ga (2p) after linear background reduction are located at BE 1117.6 eV and 1144.5 eV, which corresponds to Ga $2p_{3/2}$ and Ga $2p_{1/2}$ energy levels. A hump at BE 1133 eV was observed between spin-orbit components, which might be related to the reported loss feature [115]. Fig. 7.3 (c) depicts the N 1s peak centered at 397 eV, which matches the literature. The N 1s peak confirms the presence of N in the deposited film as the observed peak is centered at BE 397 eV, which is different from the BE of atmospheric N_2, i.e., 406 eV [116]. To further confirm the formation of the Mn_3GaN film, we have collected XANES spectra.

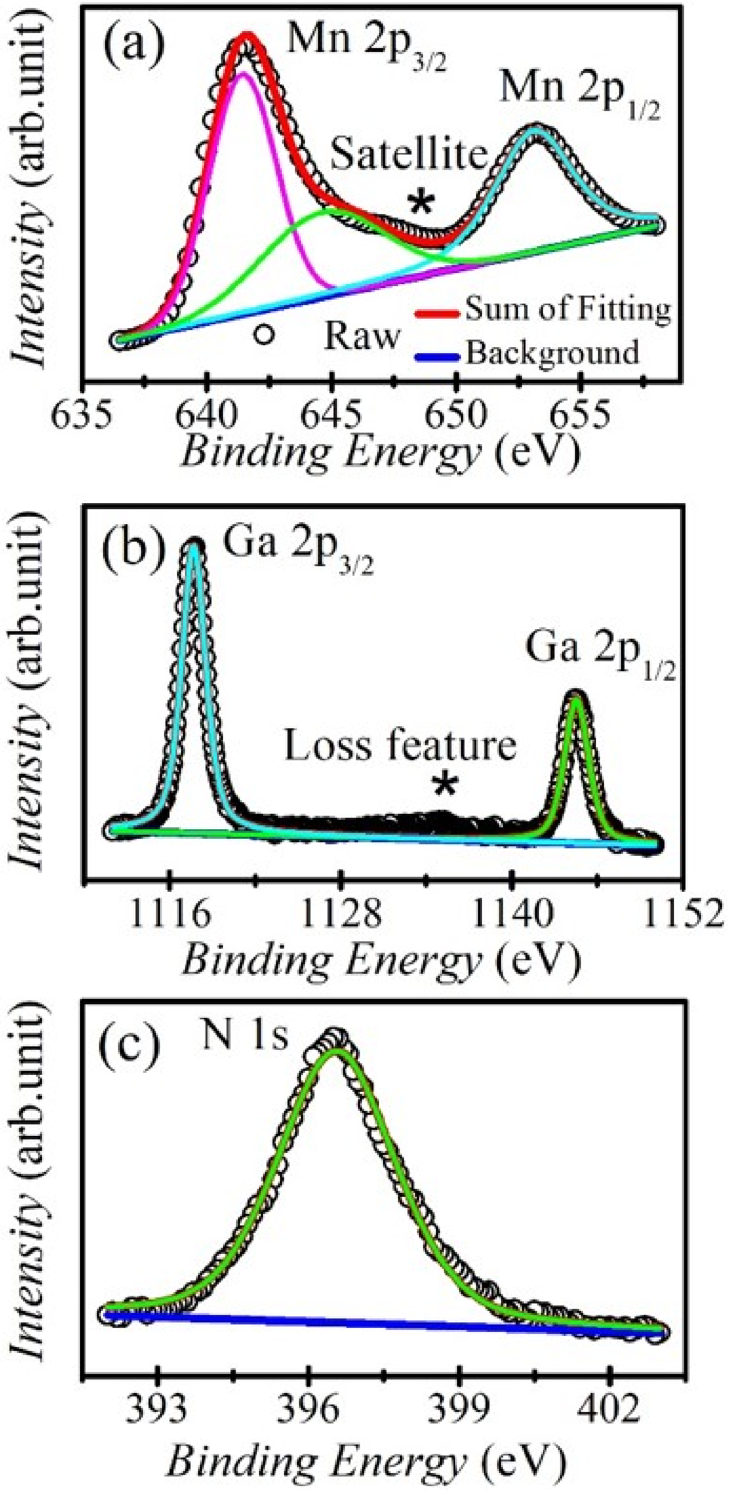

Figure 7.3: (a)-(c) Mn-2p, Ga-2p, and N_2-1s peaks observed in XPS data of the thin film Mn_3GaN compound.

7.2.5 XANES analysis

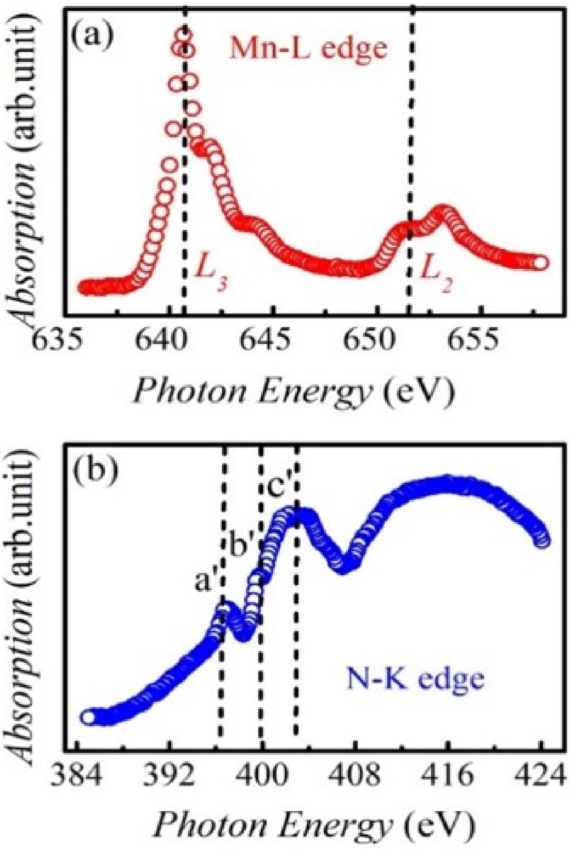

Figure 7.4: (a) and (b) Mn L-edge and N K-edge XANES spectra of the thin film Mn3GaN compound, collected using the total electron yield mode.

The XANES spectra are shown in Fig. 7.4 (a) and (b). Fig. 7.4 (a) shows the spectra of the Mn L-edge, well matched with the spectra reported for the Mn_3GaN [117]. The Mn L3 and L2 edges centered at photon energy 640.6 eV and 651.4 eV, respectively, can confirm the oxidation state of Mn, which is consistent with the Mn^{+2} ion, as reported in the literature for MnO [117]. This is also in good agreement with the XPS result. Fig. 7.4 (b) indicates the N K-edge centered at photon energies 397.5 eV, 399.4 eV, and 402.7 eV, represented by a’,b’, and c’. The first feature a’ matches with N K-edge for η-Mn3N2 [118]. The subsequent features b’ and c’ are most likely arising from two distinct N metal bond types, such as π-(p_z) along the c axis and σ-(p_{xy}) in the ab plane, well matching with reported N K-edge of GaN [119]. Hence, both XPS and XANES spectra confirm the presence of nitrogen in our Mn_3GaN thin film.

7.2.6 Resistivity analysis

Bulk stoichiometric Mn_3GaN is known to undergo a first-order phase transition from the paramagnetic (PM) to a geometrically frustrated non-collinear triangular AFM (AFT) phase in Γ^{5g} symmetry [66] at T_N, which is reported to lie in the range ∼290 K [26] to ∼270 K [62, 66] for the ’stoichiometric’ samples, depending on the measurement technique employed. This transition is accompanied with a large negative linear thermal expansion coefficient $\alpha \sim -25 \times 10^{-6}$ K_{-1} [15]. A recent powder neutron scattering study has revealed that the onset of this phase transition occurs at ∼270 K but is completed at ∼220 K with the coexistence of PM and AFM phases in the temperature range of ∼270 K to ∼220 K. The AFM single phase is stable down to ∼120 K, below which it begins to transform to a ferrimagnetic M-1 phase even as the large fraction of AFM phase continues to coexist down to the lowest temperature ∼75 K with gradually decreasing phase fraction [66].

The signatures of the above-mentioned sequence of magnetic transitions [66] are observed in the temperature dependence of the resistivity (ρ_{xx}-T plot) shown in Fig. 7.5. It reveals a high-temperature metal-to-insulator transition (MIT) and insulator-to-metal (IMT) transition at ∼275 K and ∼225 K during heating, respectively, which correlate well with the onset of the PM to the Γ^{5g} antiferromagnetic (AFM) transition and completion of the conversion of the coexisting PM phase into the AFM phase, respectively [66]. Apparently, the phase coexistence increases the resistivity in the 275-220 K range due to enhanced electron scattering from the PM-AFM interfaces [69, 70]. We observe a thermal hysteresis of ∼1.6 K [see inset (i) of Fig. 7.5], which along with the coexistence of the PM and AFM phases, confirms the first-order character of the PM to AFM transition. On application of a high magnetic field of 8 T, the transition temperature is slightly shifted towards the lower temperature side from 275 K to 272 K [see inset (ii) of Fig. 7.5], which is consistent with suppression of magnetic transition in the geometrically frustrated antiferromagnets under field [71].

The ρ_{xx}-T plot in the pure AFM Γ^{5g} phase below ∼225 K shows metal-like behavior in the sense that the ρ_{xx} decreases with temperature. The onset of the AFM Γ^{5g} to the ferrimagnetic M-1 [66] at ∼120 K is signalled by a change in curvature of the ρ_{xx}-T plot, as revealed by the anomaly in the first and second derivatives of resistivity with respect to temperature at ∼120 K (see Fig. 7.6 and inset of Fig. 7.6, respectively). Not only the resistivity shows an anomaly at the onset of the AFM Γ^{5g}

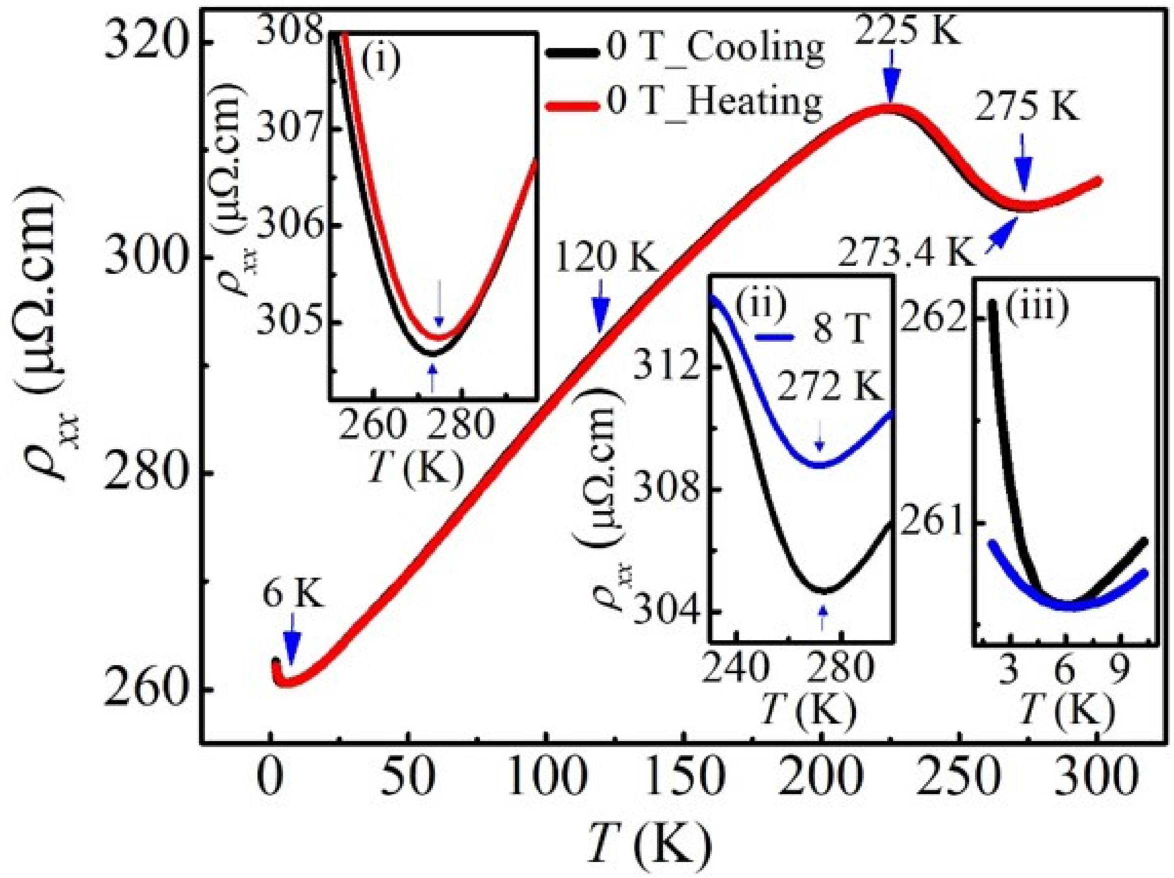

Figure 7.5: Temperature-dependent resistivity data at zero field in both cooling and heating cycle. Inset (i) shows the zoomed view of high temperature thermal hysteresis. Inset (ii) shows the slight shift in transition temperature in the presence of high magnetic field of 8 T as compared to the zero field. Inset (iii) shows the zoomed view of the temperature-dependent resistivity data in the low-temperature region at 0 T and 8 T magnetic fields.

to the ferrimagnetic M-1 phase transition at ∼120 K, but temperature-dependent magnetization data (M-T) at 3 T magnetic field (corrected for the diamagnetic contribution from the Si substrate) also shows an anomaly in the first derivative of magnetization with respect to temperature, as depicted in the inset of Fig. 7.7 (a), which further confirms the coupling of the diverse degrees of freedom.

The evolution of a ferro/ferri-magnetic-like rise in M-T data below 75 K may occur due to the appearance of the large percentage (∼80%) of the ferrimagnetic M-1 phase, as reported in the neutron diffraction study [66]. The magnetic field-dependent magnetization data (corrected for the diamagnetic contribution from the Si substrate) [Fig. 7.7 (b)] also shows a sharp increase in magnetization at higher fields (around 5 T) in the same temperature regime below 75 K due to the appearance of the ferrimagnetic phase. The broad hump in the M-T plot at ∼40 K in Fig. 7.7 (a) is known to arise

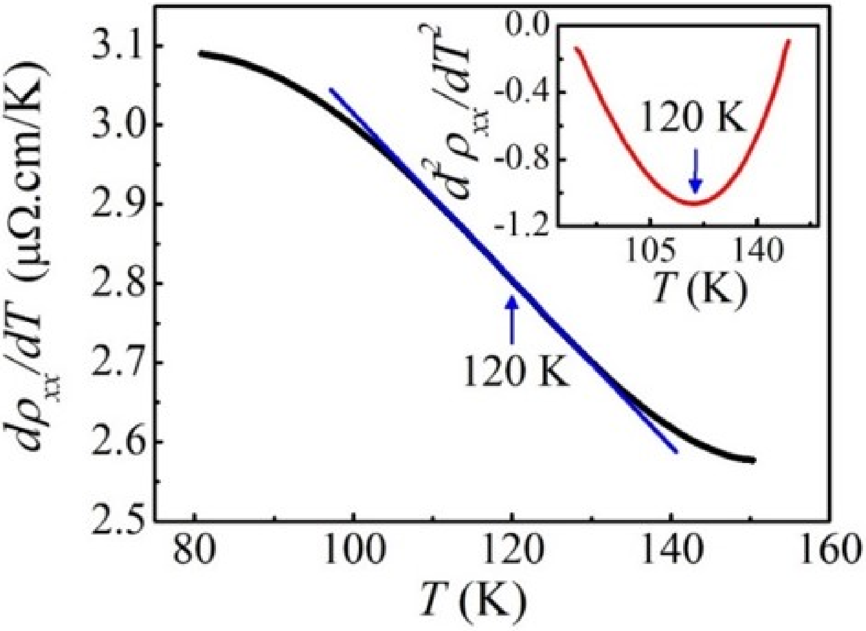

Figure 7.6: The first derivative of resistivity with respect to temperature. Inset shows the second derivative of resistivity with respect to temperature.

due to spin disorder resulting from some Mn atoms occupying the Ga sites [62], presumably because of the loss of Ga due to its low vapour pressure. This broad peak shifts systematically to a higher temperature side with increasing anti-site disorder at the Ga site [62].

Comparing the broad hump temperature in Fig. 7.7 (a) with the published phase diagram [62] of Mn$_{4-x}$Ga$_x$N as a function of x shows that in our samples, there may be 5% Mn at the Ga site. This hump is followed by a sharp increase in magnetization with further lowering of the temperature, presumably due to dominant ferromagnetic contributions [72].

The metal-like behavior of ρ_{xx} with temperature in both the AFM Γ^{5g} and the ferrimagnetic tetragonal M-1 phases is primarily due to the interaction between electrons and phonons (e-ph). Accordingly, we analyzed the ρ_{xx}-T data in the range 190-30 K using the Bloch-Grüneisen relation [73]:

$$\rho_{\text{xx}} = \rho_0 + \rho_{\text{e-ph}} \left(\frac{T}{\theta_D}\right)^5 \int_0^{\frac{\theta_D}{T}} \frac{x^5}{(e^x - 1)(1 - e^{-x})} dx \tag{7.1}$$

where ρ_0 and $\rho_{\text{e-ph}}$ represent the residual resistivity and proportionality constant for the electron-phonon scattering term, respectively, while θ_D is the Debye temperature. The fit is rather poor, as can be seen from Fig. 7.9. The misfits in the temperature ranges 190-130 K and 75-30 K, representative

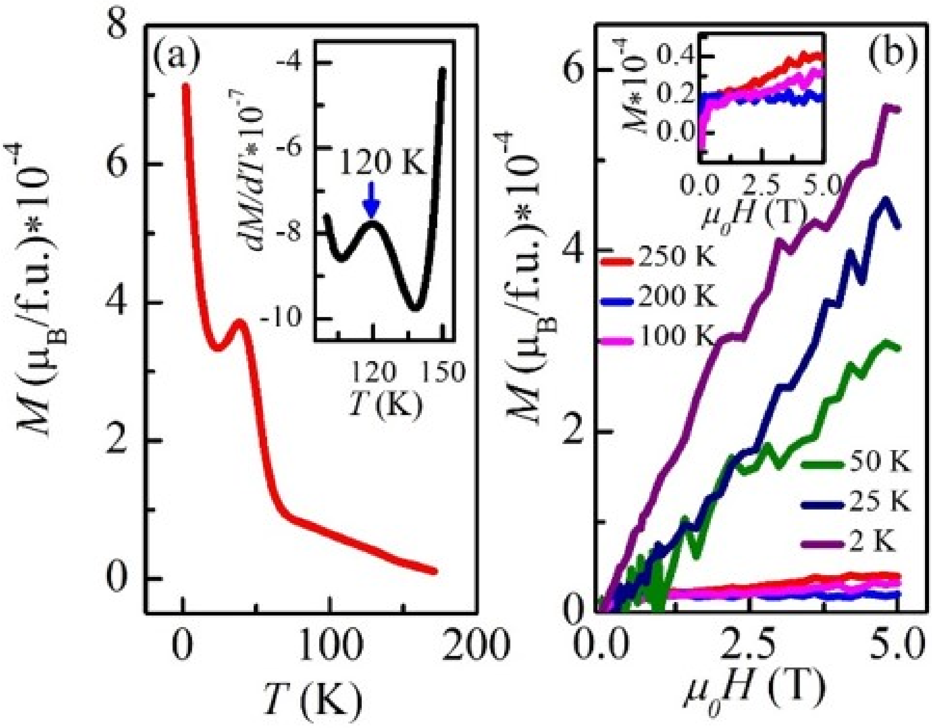

Figure 7.7: (a) Temperature-dependent magnetization curve at 3 T magnetic field of Mn$_3$GaN thin film. Inset shows the derivative of magnetization with respect to temperature. (b) Isothermal magnetization versus field data at different temperatures. Inset shows a zoomed view of the M-H data above 50 K.

of the single-phase AFM Γ^{5g} and predominantly ($\sim$80% as per [66]) ferrimagnetic M-1 phase, are shown more clearly in the insets (i) and (ii) of Fig. 7.9, respectively.

The analysis of the ρ_{xx}-T data in the two temperature ranges separately using Eq. 7.1 led to excellent fits for both regions, as shown in Figs. 7.8 (a) and 7.8 (b). The best fit parameters for the AFM Γ^{5g} and the predominantly ($\sim$80% as per [66]) ferrimagnetic M-1 phases are $\rho_0 = 2.7\times10^{-4}$ Ω.cm, $\rho_{\text{e-ph}} = 2.4\times10^{-4}$ Ω.cm, θ_D = 276 K and $\rho_0 = 2.6\times10^{-4}$ Ω.cm, $\rho_{\text{e-ph}} = 1.7\times10^{-4}$ Ω.cm, θ_D = 170 K, respectively. The difference in the $\rho_{\text{e-ph}}$ and θ_D values in the AFM Γ^{5g} and the ferrimagnetic M-1 phases clearly reveals the presence of a complex interplay of the lattice, electronic and spin degrees of freedom [74] in Mn$_3$GaN as the magnetic structure changes.

Below $\sim$30 K, the ρ_{xx}-T plot begins to show departures from the Bloch-Grüneisen model and eventually leads to a second MIT-like upturn at $\sim$6 K, as can be seen from Fig. 7.5 and the inset (iii) of Fig. 7.5. This M-I transition is not linked with any LRO magnetic transitions unlike those at $\sim$225 K and 75 K [71]. Such a low-temperature upturn can be caused by Kondo effect [38], weak localization (WL) [75], and electron-electron interaction (EEI) [76, 77, 78]. The Kondo effect arises due to

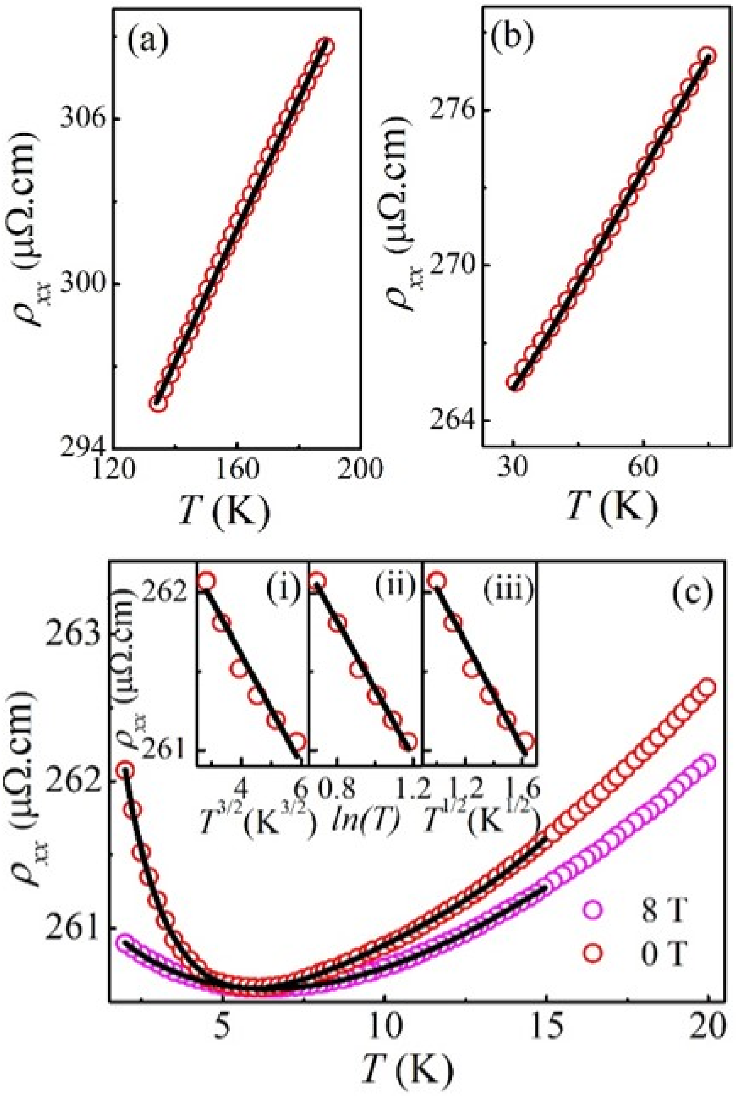

Figure 7.8: Fitting of resistivity versus temperature data using Eq. (7.1) in temperature range (a) 190-130 K and (b) 75-30 K. (c) Fitting of the resistivity minima behaviour using Eq. (2) below 15 K at 0 T and 8 T magnetic fields. The inset (i), (ii), and (iii) indicates the fitting up to 3 K by considering weak localization effect, Kondo effect, and localized electron-electron interaction, respectively. The continuous black line indicates the fitted curve.

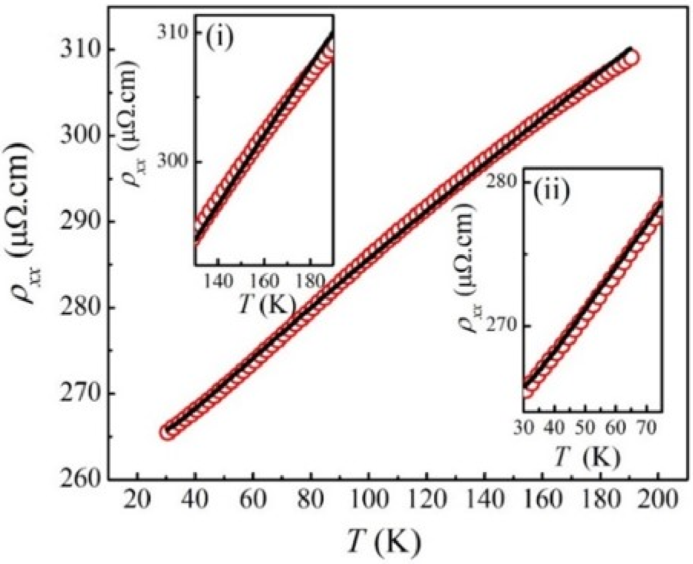

Figure 7.9: Fitting of resistivity versus temperature data using Eq. (7.1) in temperature range 190-30 K. Insets (i) and (ii) shows the zoomed view of misfit in the temperature range 190-130 K and 75-30 K, respectively.

antiferromagnetic exchange coupling between the delocalized conduction electrons and localized 3d spins associated with the magnetic impurity atoms [38, 39]]. WL effect has been generally observed in weakly disordered systems wherein disorder/defects can affect the motion of conduction electrons and give rise to the localization effects and, hence, insulating behavior [48, 79].

The EEI, on the other hand, has been attributed to interference among the electron waves resulting from the interaction between conduction electrons and their elastic scattering by static inhomogeneities or defects in metals [48, 75, 76, 79, 80]. The energy scales associated with these processes are such that they become effective at rather low temperatures. To understand the genesis of the low-temperature upturn in the ρ_{xx}-T plot of Mn_3GaN in Fig.1, we first considered separately the contributions with WL showing $\rho_{xx} \propto -T^{3/2}$ dependence [inset (i) of Fig. 7.8 (c)] for a 3D disordered system [48, 81, 82, 83], the Kondo effect showing $\rho_{xx} \propto$ -lnT dependence [inset (ii) of Fig. 7.8 (c)] [75, 80] and the EEI which shows $\rho_{xx} \propto -T^{1/2}$ dependence [see inset (iii) in Fig. 7.8 (c)]. The fit for the Kondo effect up to ∼3 K is better than that for the EEI and WL [see the zoomed view in Figs. 7.10 (a), (b) and (c)]. By including the electron-electron interaction (EEI) term along with the Kondo term, a good fit is observed up to resistivity minima T_{min} ∼6 K, as shown in Fig. 7.11 (a) suggesting the contributions from both the factors in the resistivity upturn. A good fit at still higher

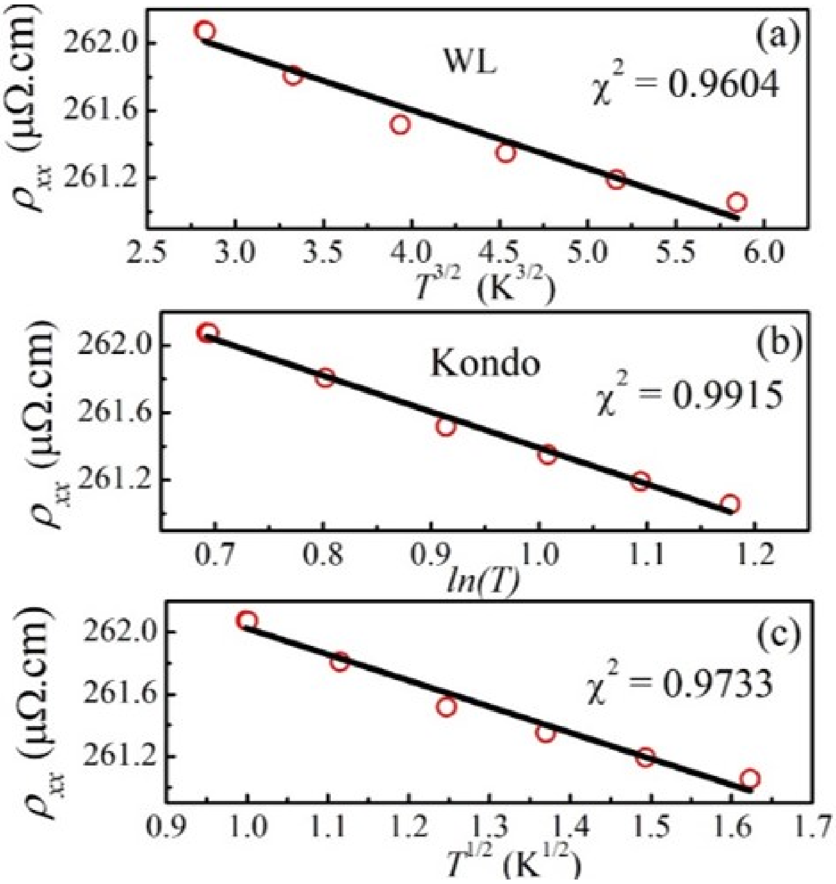

Figure 7.10: (a), (b), and (c) Linear fitting of the resistivity data with respect to $T^{3/2}$, ln(T) and $T^{1/2}$ by considering weak localization, Kondo scattering and electron-electron scattering mechanisms, respectively.

temperatures up to ~10 K can be obtained by considering inclusion of the Fermi liquid term ($\rho_{xx} \propto T^2$) [84], as can be seen from Fig. 7.11 (b). The Fermi liquid (FL) behavior is expected due to the delocalized electron-electron correlations [85] above the resistivity upturn temperature as a precursor spin-flip scattering [86]. Finally, a very good fit up to ~15 K was obtained by incorporating the electron-phonon contribution, which varies as $\rho_{xx} \propto T^5$ at low temperatures [87]. Therefore, we have fitted the overall resistivity behavior in the temperature range of 2-15 K using the following equation:

$$\rho_{xx}(T) = \rho_0 - \rho_{\text{k}}.lnT + \rho_{\text{e-e}}.T^{1/2} + \rho_{\text{fl}}.T^2 + \rho_{\text{e-ph}}.T^5 \tag{7.2}$$

where ρ_0, ρ_{k}, $\rho_{\text{e-e}}$, ρ_{fl}, and $\rho_{\text{e-ph}}$ are residual resistivity, Kondo-like spin-dependent scattering coefficient, EEI coefficient, electron-electron correlation coefficient described by FL theory and electron-

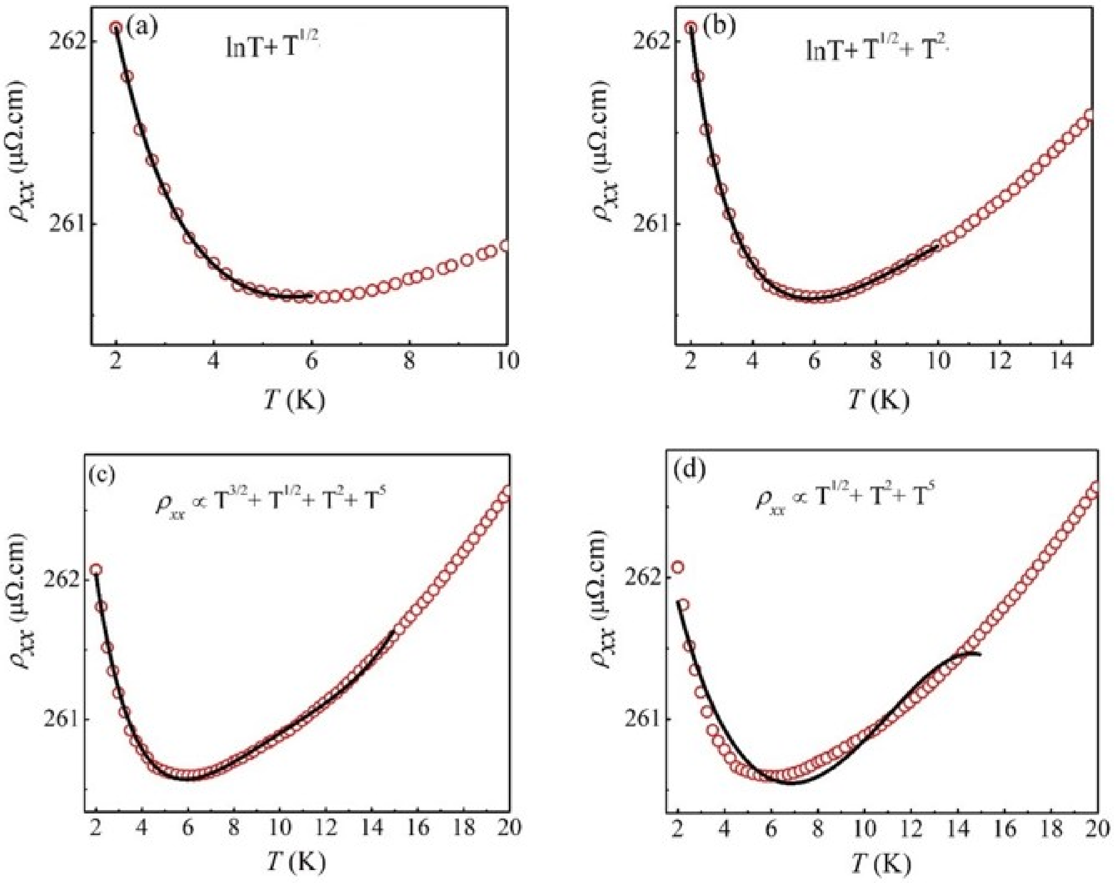

Figure 7.11: (a) Fitting of the observed upturn in resistivity below 6 K at zero magnetic field considering Kondo and electron-electron coupling terms. (b) Fitting of the observed minima in resistivity up to 10 K considering Kondo, electron-electron coupling, and Fermi liquid terms. (c) Fitting of the observed minima up to 15 K considering weak localization, electron-electron coupling, Fermi liquid and electron-phonon interaction terms. (d) Fitting of the minima up to 15 K considering only electron-electron coupling, Fermi liquid and electron-phonon interaction terms.

phonon scattering coefficient, respectively. The data at zero magnetic field fits very well with Eq. (7.2), as can be seen from Fig. 7.8 (c). The coefficients ρ_k, $\rho_{e\text{-}e}$, ρ_{fl}, and $\rho_{e\text{-}ph}$ for the best fit are 7.6×10^{-6}, 7×10^{-6} Ω.cm/K$^{-1/2}$, -1.5×10^{-8} Ω.cm/K^{-2}, and 1×10^{-12} Ω.cm/K^{-5}, respectively. These values indicate that the Kondo effect has the dominant contribution followed by the EEI contribution over the other terms. It is well known that the Kondo scattering is suppressed at higher magnetic fields because of the weakening of the spin-flip scattering [54, 88] due to $g\mu_B H >> k_B T_k$, where T_k is the Kondo temperature, which is defined as the onset temperature for the logarithmic upturn [89]. The T_k can be estimated from the ρ_{xx}(T) plot, which has the dominant contribution of the Kondo effect and electron-electron scattering mechanism. The differential of the ρ_{xx}-T [90] with only the Kondo and EEI terms results in $T_k = (2\rho_k/\rho_{e\text{-}e})^2 = 5.5$ K, obtained from the value of coefficients $\rho_\mathrm{k} = 6.5\times10^{-6}$ and $\rho_\text{e-e} = 5.5\times10^{-6}$ Ω.cm/K$^{-1/2}$ for the fit shown in Fig. 7.11 (a), which is very close to the T$_\mathrm{min}$ ($\sim$6 K) at zero magnetic field though not exactly the same [48]. Since the EEI contribution is field independent [77] while the Kondo contribution is field dependent, we also analyzed the ρ_xx-T data at a field of 8 T applied along the z-direction for which gμ_BH >> k$_\mathrm{B}$T$_\mathrm{k}$. We find that ρ_xx-T data at 8 T is well fitted using Eq. (7.2) without considering the Kondo contribution, as can be seen from Fig. 7.8 (c). The coefficients obtained from this fit are $\rho_\text{e-e}$ = -5.7$\times10^{-7}$ Ω.cm/K$^{-1/2}$, $\rho_\mathrm{fl} = 8.9\times10^{-9}$ Ω.cm/K^{-2}, and $\rho_\text{e-ph}$ = -2.5$\times10^{-13}$ Ω.cm/K^{-5}. This clearly shows that the Kondo contribution is getting suppressed at the higher magnetic field, making EEI the dominant contributor to the resistivity upturn, as expected [54, 91]. Fits at 0 T field involving WL term instead of Kondo term in Eq. (7.2) were found to be less satisfactory (see Fig. 7.11 (c)). Further, dropping the Kondo or WL terms altogether in Eq. (7.2) led to far worse fits (see Fig. 7.11 (d)). All these clearly indicate that the main contributors to the resistivity upturn below $\sim$6 K in zero magnetic field are the Kondo scattering and EEI, the former being the dominant one.

In order to rule out the WL contribution to the resistivity upturn convincingly and confirm the presence of the dominant Kondo effect unambiguously, we analyzed the resistivity data measured with the magnetic field (ρ_xx-H) applied perpendicular to the plane of the thin film at selected temperatures and calculated the magnetoresistance (M.R.) using the relationship [92]:

$$M.R. = \frac{\rho_{xx}(H) - \rho_{xx}(H=0)}{\rho_{xx}(H=0)} \tag{7.3}$$

Fig. 7.12 (a) shows the M.R. at different temperatures. The M.R. is either positive or negative in the entire magnetic field region at temperatures (250 K, 200 K, and 50 K), well above the resistivity minimum, depending upon the type of spin ordering. In the temperature range 275-220 K, where the PM and AFM phases coexist [66], the M.R. is found to be positive due to AFM spin ordering within the PM phase, as illustrated in Fig. 7.12 (a) for 250 K. In the pure AFM regime from 220-120 K also, the M.R. is positive, but its magnitude is much less than that in the PM + AFM coexistence regime, as can be seen from a comparison of the M.R. values at 250 K and 200 K, which might be observed due to pure AFM ordering at 200 K as per the neutron scattering results [66]. The underlying mechanism behind the observed positive M.R. is that the application of an external magnetic field suppresses

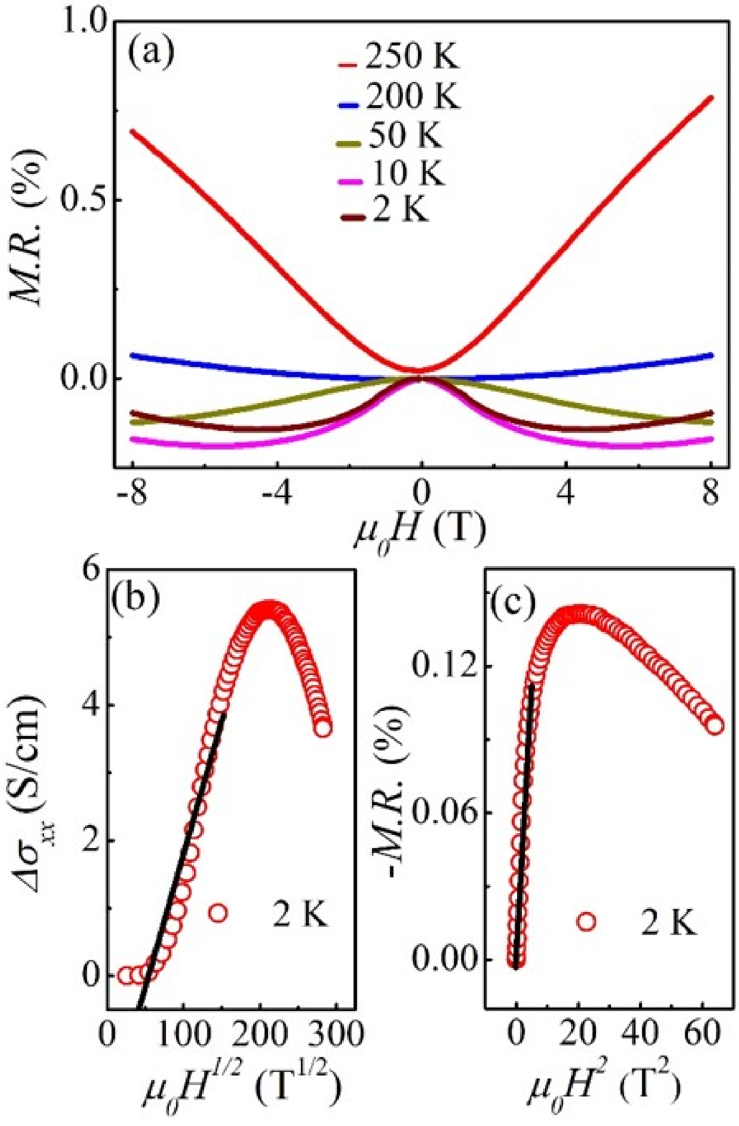

Figure 7.12: (a) Magnetoresistance data at different temperatures. (b) and (c) show fitting of low-field magnetoconductivity and magnetoresistance data using Eq. (7.4) and (7.5), respectively. The continuous black line indicates the fitted curve.

the long-range antiferromagnetic order, leading to the emergence of short-range antiferromagnetic fluctuations [93]. These fluctuations enhance electronic scattering, which ultimately results in an increase in resistivity with the magnetic field. In the temperature regime where the ferrimagnetic M-1 phase dominates, the M.R. is found to have a negative value, as illustrated in Fig. 7.12 (a) at 50 K. The negative M.R. arises due to the reduction in electronic scattering due to the magnetic field-induced enhanced spin ordering [93]. As we move towards lower temperatures below 50 K, we observe non-monotonic negative M.R. behavior, which increases at lower fields but starts decreasing at higher fields. Such a negative M.R. below the resistivity upturn temperature can in principle arise due to either WL or Kondo effect with subtle differences [94]. One expects a cusp-like behavior around zero field for WL whose absence in Fig. 7.12(a) makes WL contribution unlikely [95]. The WL and Kondo effect-driven magnetoconductivity ($\Delta\sigma_{\mathrm{xx}}$) and M.R. have different field dependence. The $\Delta\sigma_{\mathrm{xx}}$ for WL in 3D systems follows the following field dependence at low fields [96, 97, 98, 99, 100]:

$$\Delta\sigma_{\mathrm{xx}}(H) = \sigma_{\mathrm{xx}}(H) - \sigma_{\mathrm{xx}}(H = 0) = C.H^{1/2} \tag{7.4}$$

where $\Delta\sigma_{\mathrm{xx}}$(H) and $\Delta\sigma_{\mathrm{xx}}$(H=0) are the magnetic field (H) dependent and zero field (H=0) conductivity, respectively, and C is a proportionality constant. The negative M.R. due to the Kondo effect, on the other hand, follows quadratic dependence at low magnetic fields [101, 102]:

$$M.R. = S(T).H^2 \tag{7.5}$$

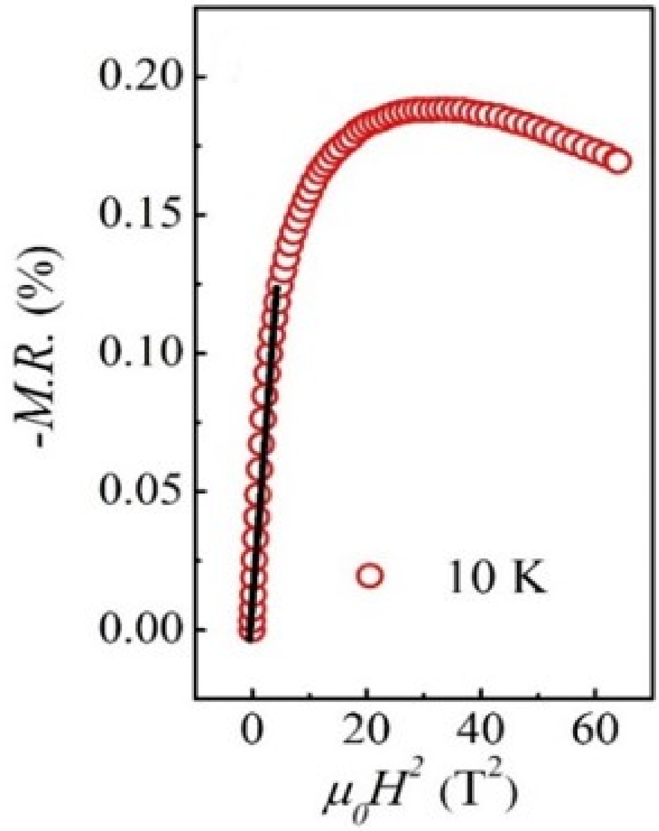

Figure 7.13: Fitting of the low-field magnetoresistance data using Eq. (7.5).

where S(T) is a temperature-dependent proportionality coefficient. Fig. 7.12 (b) and 7.12 (c) depict the fits to Eqs. (7.4) and (7.5), respectively. It is evident that the negative M.R. at 2 K is best explained by the Kondo effect and not the WL effect up to 3 T. In a Kondo system, the magnetic field reduces the fluctuations in localized magnetic moments and spin-dependent scattering, resulting in a negative M.R. [94, 103]. However, when the magnetic field strength exceeds a critical value, the exchange interaction between conduction electrons and magnetic impurities becomes weaker as compared to k_BT_k, leading to the destabilization of Kondo screening [88]. This nonmonotonic negative MR persists even at 10 K (see Fig. 7.13), confirming the presence of precursor spin-flip scattering above the Kondo minimum temperature also.

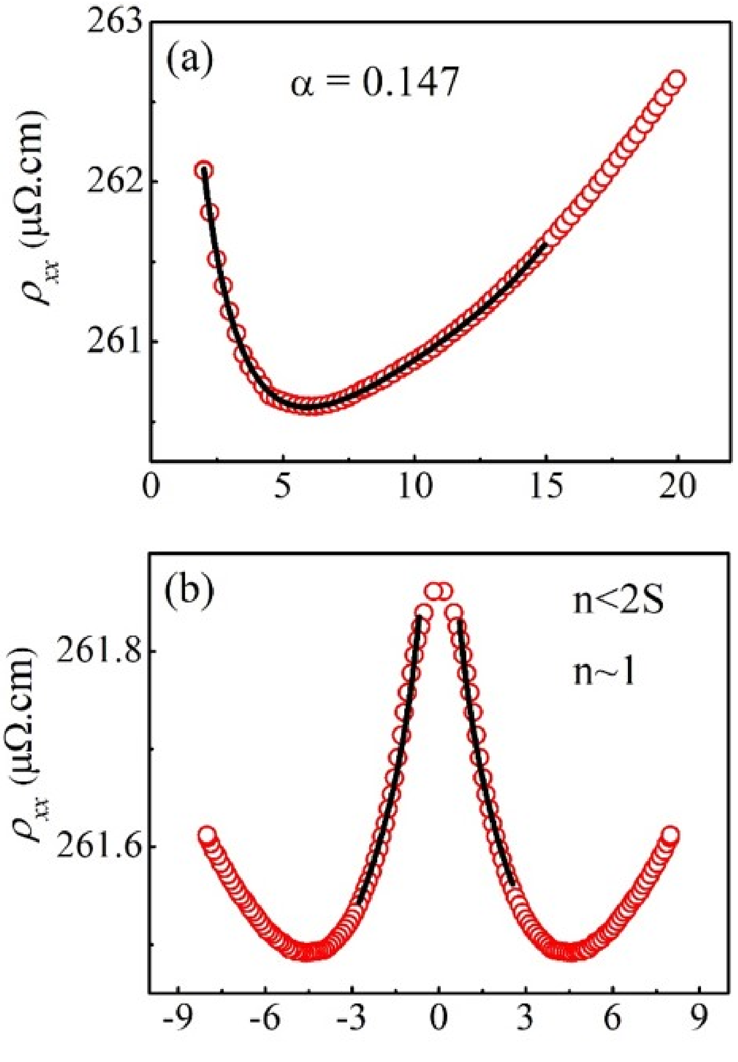

Figure 7.14: (a) Fitting of resistivity versus temperature data at zero field in the low-temperature region by using empirical relation derived from numerical renormalization group (NRG) calculation. (b) Fitting of magnetic field dependent resistivity data in low magnetic field region < 3 T at 2 K by following NRG n-channel Kondo model. The continuous black line indicates the fitted curve.

The local spin-dependent scattering ρ_s(T) for a Kondo system using the approach of numerical renormalization group (NRG) method, can be expressed as [104]:

$$\rho_s(T) = \rho_s(0)[1 + (2^{1/\alpha} - 1)(T/T_K)^2]^{-\alpha} \tag{7.6}$$

where α is a parameter related to the steepness of the ρ_{xx}-T plot below the upturn temperature and ρ_{s}(0) is the coefficient of spin-dependent scattering. Even after replacing the lnT Kondo term in Eq. (7.2) with the above empirical expression in Eq. (7.6) for spin-dependent scattering, the zero field resistivity data shows an excellent fit for $\mathrm{T_k}$ $\sim$5.5 K, estimated from the differential resistivity from fits below 6 K using Kondo and EEI terms [Fig. 7.14 (a)]. The value of α and the coefficient ρ_{s}(0) obtained for this $\mathrm{T_k}$ are 0.146 and 3.0×10^{-7}, respectively. The value of α suggests local spin moment S = 3/2 [104, 105] for the Mn atoms at the Ga site.

The local spin S = 3/2 can interact with the conduction electrons through n different orbital channels, where n = 2S. The ground state of the Kondo system is decided by the extent of screening of the isolated magnetic spin by the conduction electrons. It is therefore of interest to explore the number of orbital channels involved in the spin-flip scattering. This was carried out by analyzing the M.R. data using the NRG n-channel Kondo model. The ρ_{xx}-H (T = 0 K) linked to spin $\pm$1/2 conduction electrons in a system containing a small concentration of Kondo spin S is expressed as [48, 104, 106]:

$$\rho_{xx}(H) = \frac{2m\pi^2 N(\omega = 0)}{n_e e^2}[Sin^2\delta_{1/2}(H) + Sin^2\delta_{-1/2}(H)]^{-1} \tag{7.7}$$

where n_e, m, and e are electron density, electron mass, and charge, respectively, while N(ω=0) is the unperturbed electron density of states per spin at the frequency ω = 0. The scattered electron phase shift $\delta_{\pm1/2}$(H) is connected to local spin magnetization M_i(H), expressed as $\delta_{\pm1/2}$(H) = π/2[1 $\pm$ 2M_i(H)] [107]. M_i(H) relies on the interplay between n and S, with each channel carrying 1/2 spin. Three situations arise: (i) n = 2S; (ii) n $>$ 2S; (iii) n $<$ 2S. In the case of n = 2S, conduction electrons fully screen the local spin. When n $>$ 2S, scattering electrons over-compensate the local spin S, leading to non-Fermi liquid behavior and possible AFM interaction [108]. On the other hand, n $<$ 2S results in an incomplete quenching of the local spin by scattering electrons, and in this case, uncompensated spins can interact via RKKY interaction, possibly resulting in a ferromagnetic ground state below Kondo temperature T$_\mathrm{k}$ [108]. For gμ_BH << k$_\mathrm{B}$T$_\mathrm{k}$, the expressions for M$_i$(H) in the above three scenarios are as follows [48, 108]:

$$M_i(H) \sim \frac{g\mu_B H}{2\pi k_B T_K} + k_1 (\frac{g\mu_B H}{2\pi k_B T_K})^3 + ...; (n = 2S) \tag{7.8}$$

$$M_i(H) \sim (S - n/2)(1 - \frac{1}{log(\frac{g\mu_B H}{2\pi k_B T_K})})......; (n < 2S) \tag{7.9}$$

$$M_i(H) \sim \sum_{k=1}^{\infty} b_k (\frac{H}{T_K})^{2k/n} + \sum_{k=0}^{\infty} c_k (\frac{H}{T_K})^{2k+1}......; (n > 2s) \tag{7.10}$$

where g, μ_B, and k_B are the g factor, Bohr magnetron, and Boltzmann constant, respectively, while k_1, b_k, and c_k are temperature and field-independent coefficients. We fitted the observed MR data in the low field limit for the three scenarios following earlier works [48, 108] and found that the best fit is obtained for n < 2S [see Fig. 7.14 (b)], and the value of the parameter n obtained after the least squares fit is 1, which indicates that the conduction electrons are unable to completely screen the spin of the magnetic impurity through the available orbital channels. The underscreened spin magnetic moments (S-n/2 > 0) could develop LRO ferromagnetism [108] via the RKKY exchange interaction at low temperatures if their concentration is above some threshold value.

As said earlier, in the Mn$_3$GaN compound, the possible anti-site Mn/Ga disorder [62] can lead to a very small fraction of Mn spins occupying the Ga sites, which may behave as magnetic impurities. These impurities further interact with the d-like conduction band states on the Mn-triangular sublattices via the Heisenberg exchange, which may be responsible for the observed Kondo effect. Varying the relative concentration of Mn and Ga in Mn$_{3+x}$Ga$_{1-x}$N may result into a larger fraction of Mn occupying the Ga sites with increasing x. This may enhance the probability of interactions between impurity spins and conduction electrons and result in the stronger Kondo effect, which may develop coherence leading to the dense Kondo lattice[59] and open an energy gap near the Fermi level, giving rise to the emergence of Kondo insulator as reported in hexagonal Mn$_{3+x}$Sn$_{1-x}$, where due to antisite disorder in which a large fraction of Mn occupying the Sn site [64]. We hope our work stimulates further studies on system Mn$_{3+x}$Ga$_{1-x}$N as a function of x in search of the Kondo insulator state.

7.2.7 Anomalous Hall analysis

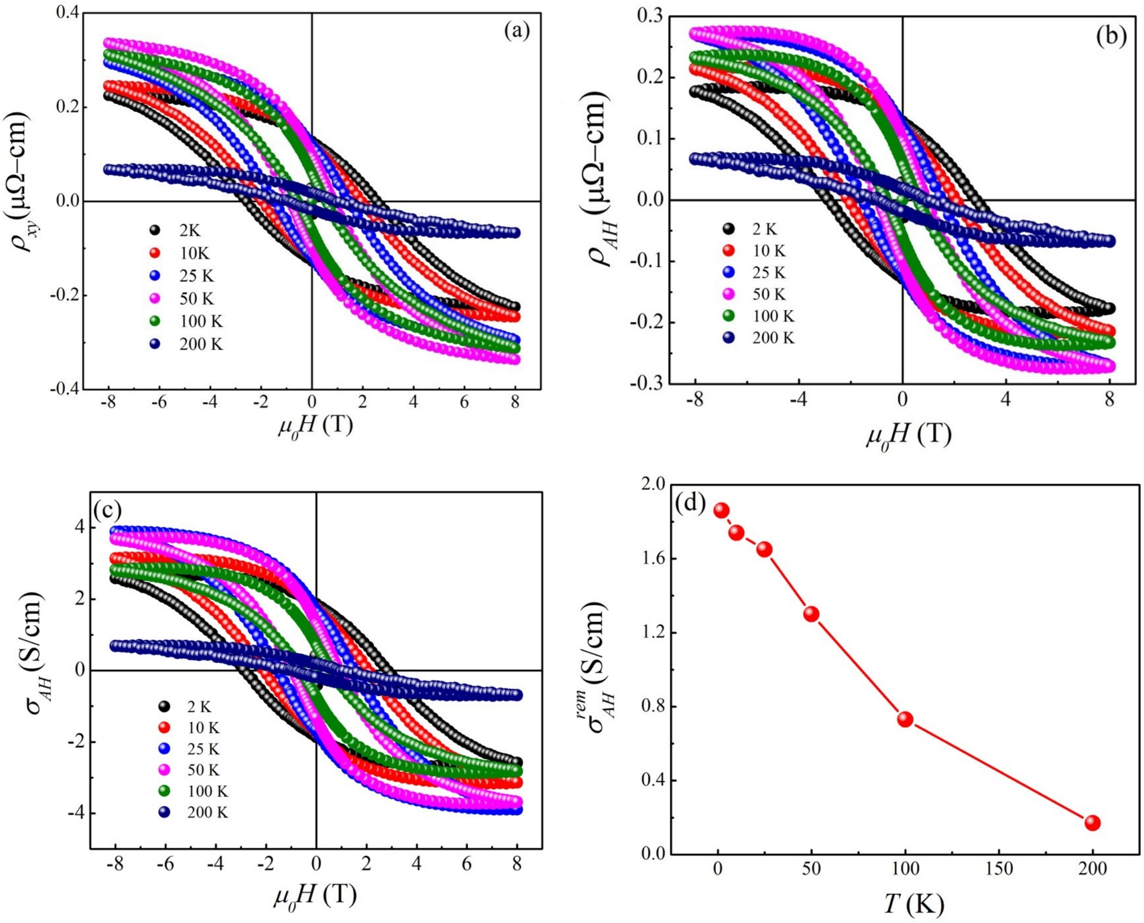

Figure 7.15: (a) Hall resistivity of the Mn$_3$GaN compound at different temperatures. (b) Anomalous Hall resistivity at different temperatures. (c) Anomalous Hall conductivity at different temperatures. (d) Variation of anomalous Hall conductivity at zero field as a function of temperature.

The Hall measurements are carried out in temperature range of 2-200 K to investigate the anomalous Hall effect in the Mn$_3$GaN compound. The Hall data is collected at different temperatures up to the magnetic field of ±8 T [Fig. 7.15 (a)], which indicates the presence of AHE. The total Hall resistivity is typically consist of two contributions,i.e., ordinary Hall and anomalous Hall [109]-

$$\rho_{\mathrm{xy}} = R_0 H + R_s M \tag{7.11}$$

where R_0 and R_s are the coefficient of ordinary Hall and anomalous Hall resistivity, respectively. To calculate the coefficients, we have fitted the high field Hall data using the above relation. Fig. 7.15 (b) shows the anomalous Hall resistivity (ρ_{AH}) after subtracting the ordinary Hall contribution from the field dependent total Hall resistivity [Fig. 7.15 (a)] by using the obtained value of ordinary Hall coefficient. We have subsequently calculated the anomalous Hall conductivity (AHC) by using the relation [110]-

$$\sigma_{\mathrm{AH}} = \frac{\rho_{\mathrm{AH}}}{{\rho_{\mathrm{H}}}^2 + {\rho_{\mathrm{xx}}}^2} \tag{7.12}$$

Fig. 7.15 (c) represents the AHC at different temperatures, which indicates that the AHE is strongly dependent on temperature. Notably, there is an hysteresis in the Hall data, whereas there is no such kind of feature observed in the M-H data. The very small magnetic moment, and the hysteretic nature of the Hall data confirm that AHE is not related to magnetization of the Mn$_3$GaN compound and is possibly related to the non-collinear AFM spin texture. A reported theoretical study suggests that the AHC in non-collinear AFM phase with Γ^{5g} magnetic symmetry will be zero and a small finite rotation from the Γ^{5g} spin configuration may give rise to the finite AHE [112]. In Fig. 7.15 (d), we have plotted the remanent AHC (AHC at zero field) as a function of temperature. We may clearly see that the AHC is maximum at 2 K and continuously decreasing with the increase in temperature and nearly vanishes at 200 K, which lies in the pure AFM Γ^{5g} region. In low-temperature region below 200 K, where the AFM Γ^{5g} and ferrimagnetic M-1 phase coexist, the AHC emerges, which may be related to the spin canting from Γ^{5g} spin configuration due to the coexisting phase of ferrimagnetic ordering [111]. Therefore, our experimental finding is consistent with previous theoretical study on the Mn$_3$GaN compound. The decrease in AHE with increase in temperature may be attributed to the variation in the angle of spin canting due to the reduction in the strength of ferrimagnetism with increasing temperature [66]. Similar temperature-dependent behavior of AHE due to variation in the angle of spin canting as a function of temperature has also been observed in a similar compound

Mn_3SnN [63].

7.3 Conclusion

In summary, we prepared a thin film sample of Mn_3GaN compound with antiperovskite structure confirmed by XRD and further characterized by various techniques such as FESEM, XPS, and XANES. The analysis of ρ_{xx}-T behavior of the thin film sample in the 300-30 K range in terms of the Bloch- Gruneisen model reveals signatures of the paramagnetic (PM) to the AFM Γ^{5g} as well as the Γ^{5g} to the ferrimagnetic M-1 transitions reported recently in a neutron diffraction study [K. Shi et al., Adv. Mater. **28**, 3761 (2016)] with different Debye temperatures for the two magnetic phases, revealing the coupling of lattice, electronic, and spin degrees of freedom. Further, the ρ_{xx}-T plot reveals an upturn below $\sim$6 K at zero magnetic field due to the combined effect of Kondo scattering and EEI, with the former being the dominant contributor. On application of a high magnetic field of 8 T, the Kondo contribution to the resistivity upturn disappears, leaving behind only the magnetic field-independent EEI contribution. Additionally, the quadratic field dependence of negative M.R. below the resistivity minimum temperature further confirms the Kondo effect and rules out WL contributions to the resistivity upturn behavior. The analysis of resistivity data in terms of the n-channel NRG model reveals that the local impurity spin is underscreened, which suggests the possibility of LRO ferromagnetic phase through RKKY interaction among the isolated magnetic spins if their concentration at the Ga sites due to anti-site disorder increases above a threshold value. It also opens the possibility of Kondo insulator behavior similar to $Mn_{3+x}Sn_{1-x}$ above a critical concentration of anti-site Mn/Ga disorder. We hope our results will stimulate further studies on this system to unravel the richness of exotic phenomena due to the coupling of lattice, electronic, and spin degrees of freedom. In addition to the exotic features in resistivity data, the Hall data reflects the presence of AHE, which might be related to a small finite rotation from the Γ^{5g} spin configuration.

References

[1] C. X. Quintela, K. Song, D.-F. Shao, L. Xie, T. Nan, T. R. Paudel, N. Campbell, X. Pan, T. Tybell, M. S. Rzchowski, E. Y. Tsymbal, S.-Y. Choi, C.-B. Eom, Epitaxial antiperovskite/perovskite

heterostructures for materials design. Sci. Adv., **6**, eaba4017 (2020).

[2] H.K. Singh, I. Samathrakis, N.M. Fortunato, J. Zemen, C. Shen, O. Gutfleisch, H. Zhang, Multifunctional antiperovskites driven by strong magnetostructural coupling. npj Comput. Mater., **7**, 98 (2021).

[3] D.-F. Shao, G. Gurung, T.R. Paudel, E.Y. Tsymbal, Electrically reversible magnetization at the antiperovskite/perovskite interface. Phys. Rev. Mater., **3**, 024405 (2019).

[4] P. Lukashev, K.D. Belashchenko, R.F. Sabirianov, Large magnetoelectric effect in ferroelectric/piezomagnetic heterostructures. Phys. Rev. B, **84** 134420 (2011).

[5] K. Kamishima, T. Goto, H. Nakagawa, N. Miura, M. Ohashi, N. Mori, T. Sasaki, T. Kanomata, Giant magnetoresistance in the intermetallic compound Mn_3GaC. Phys. Rev. B, **63** 024426 (2000).

[6] K. Asano, K. Koyama, K. Takenaka, Magnetostriction in Mn_3CuN, Appl. Phys. Lett., **92** 161909 (2008).

[7] T. Tohei, H. Wada, T. Kanomata, Negative magnetocaloric effect at the antiferromagnetic to ferromagnetic transition of Mn_3GaC, J. Appl. Phys., **94** 1800-1802 (2003).

[8] K. Takenaka, T. Shibayama, D. Kasugai, T. Shimizu, Giant Field-Induced Distortion in Mn_3SbN at Room Temperature, Jpn. J. Appl. Phys., **51** 043001 (2012).

[9] B. S. Wang, P. Tong, Y. P. Sun, X. Luo, X. B. Zhu, G. Li, X.D. Zhu, S.B. Zhang, Z. R. Yang, W. H. Song, J. M. Dai, Large magnetic entropy change near room temperature in antipervoskite $SnCMn_3$. EPL (Europhys. Lett.), **85** 47004 (2009).

[10] J. Zheng, B. Perry, Y. Wu, Antiperovskite Superionic Conductors: A Critical Review. ACS Materials Au, **1** 92-106 (2021).

[11] Y. Zhao, L.L. Daemen, Superionic conductivity in lithium-rich anti-perovskites. J. Am. Chem. Soc., **134** 15042-15047 (2012).

[12] H. Fanga and P. Jenaa, Li-rich antiperovskite superionic conductors based on cluster ions. Proc. Natl. Acad. Sci, **114**, 11046-11051 (2017).

[13] T. He, Q. Huang, A. P. Ramirez, Y. Wang, K. A. Regan, N. Rogado, M. A. Hayward, M. K. Haas, J. S. Slusky, K. Inumara, H. W. Zandbergen, N. P. Ong and R. J. Cava, Superconductivity in the non-oxide perovskite $MgCNi_3$. Nat. lett., **411** 54-56 (2001).

[14] M. Uehara, A. Uehara, K. Kozawa, Y. Kimishima, New Antiperovskite-Type Superconductor $ZnNyNi_3$. J. Phys. Soc. Japan, **78** 033702 (2009).

[15] K. Takenaka, H. Takagi, Giant negative thermal expansion in Ge-doped anti-perovskite manganese nitrides. Appl. Phys. Lett., **87** 261902 (2005).

[16] K. Takenaka, T. Hamada, D. Kasugai, N. Sugimoto, Tailoring thermal expansion in metal matrix composites blended by antiperovskite manganese nitrides exhibiting giant negative thermal expansion. J. Appl. Phys., **112** 083517 (2012).

[17] R. Huang, L. Li, F. Cai, X. Xu, L. Qian, Low-temperature negative thermal expansion of the antiperovskite manganese nitride Mn_3CuN codoped with Ge and Si. Appl. Phys. Lett., **93** 081902 (2008).

[18] J. Tan, R. Huang, W. Wang, W. Li, Y. Zhao, S. Li, Y. Han, C. Huang, L. Li, Broad negative thermal expansion operation-temperature window in antiperovskite manganese nitride with small crystallites. Nano Res., **8** 2302-2307 (2015).

[19] Y. Zhu, G. Chen, Y. Zhong, Y. Chen, N. Ma, W. Zhou, Z. Shao, A surface-modified antiperovskite as an electrocatalyst for water oxidation. Nat. Commun., **9** 2326 (2018).

[20] P.F. Li, Y.Y. Tang, W.Q. Liao, P.P. Shi, X.N. Hua, Y. Zhang, Z. Wei, H. Cai, R.G. Xiong, Experimental Evidence for a Triboluminescent Antiperovskite Ferroelectric: Tris(trimethylammonium) catena-Tri-mu-chloro-manganate(II) Tetrachloromanganate(II). Angew Chem Int Ed Engl, **57** 11939-11942 (2018).

[21] Z. Yu, H. Peng, Q. Wei, T. Huang, S. Yao, Y. Tian, C. Peng, B. Zou, The magnetic polaron modulated luminescence bands of organic-inorganic hybrid ferroelectric anti-perovskite $(C_3H_9N)_3Cd_2C_l7$ doped with Mn^2+. Mater. Today Chem., **24** 100781 (2022).

[22] B.Y. Qu, B.C. Pan, Nature of the negative thermal expansion in antiperovskite compound Mn_3ZnN. J. Appl. Phys., **108** 113920 (2010).

[23] T. Hamada, K. Takenaka, Giant negative thermal expansion in antiperovskite manganese nitrides. J. Appl. Phys., **109** 07E309 (2011).

[24] H. Lu, Y. Sun, K. Shi, J. Cui, H. Han, C. Wang, Negative thermal expansion, magnetic and electronic transport properties in antiperovskite compounds $Mn_3Ga_{1-x}Ag_xN$ ($0 \leq x \leq 1.0$). J. Magn. Magn. Mater., **514** 167137 (2020).

[25] S. Tan, C. Gao, C. Wang, T. Zhou, G. Yin, M. Sun, F. Xing, R. Cao, Y. Sun, The tunable negative thermal expansion covering a wide temperature range around room temperature in Sn, Mn co-substituted Mn(3)ZnN. Dalton. Trans., **49** 10407-10412 (2020).

[26] K. Takenaka, M. Ichigo, T. Hamada, A. Ozawa, T. Shibayama, T. Inagaki, K. Asano, Magnetovolume effects in manganese nitrides with antiperovskite structure. Sci. Technol. Adv. Mater., **15** 015009 (2014).

[27] D. Matsunami, A. Fujita, K. Takenaka, M. Kano, Giant barocaloric effect enhanced by the frustration of the antiferromagnetic phase in Mn_3GaN, Nat. Mater., **14** 73-78 (2015).

[28] D. Boldrin, I. Samathrakis, J. Zemen, A. Mihai, B. Zou, F. Johnson, B.D. Esser, D.W. McComb, P.K. Petrov, H. Zhang, L.F. Cohen, Anomalous Hall effect in noncollinear antiferromagnetic Mn_3NiN thin films, Phys. Rev. Mater., **3** 094409 (2019).

[29] K. Zhao, T. Hajiri, H. Chen, R. Miki, H. Asano, P. Gegenwart, Anomalous Hall effect in the noncollinear antiferromagnetic antiperovskite $Mn_3Ni_{1-x}Cu_xN$, Phys. Rev. B, **100**, 045109 (2019).

[30] G. Gurung, D.-F. Shao, T.R. Paudel, E.Y. Tsymbal, Anomalous Hall conductivity of noncollinear magnetic antiperovskites. Phys. Rev. Mater., **3** 044409 (2019).

[31] D. Huang, H. Li, X. Xi, J. Gao, Y.C. Lau, W. Wang, Magnetoresistance reversals and anomalous Hall effect in Mn(3)SnC and effects of carbon deficiency, J. Phys. Condens. Matter., **35** 025702 (2023).

[32] Y. You, H. Lam, C. Wan, C. Wan, W. Zhu, L. Han, H. Bai, Y. Zhou, L. Qiao, T. Chen, F. Pan, J. Liu, C. Song, Anomalous Nernst Effect in an Antiperovskite Antiferromagnet. Phys. Rev. Appl., **18** 024007 (2022).

[33] X. Zhou, J.-P. Hanke, W. Feng, S. Blügel, Y. Mokrousov, Y. Yao, Giant anomalous Nernst effect in noncollinear antiferromagnetic Mn-based antiperovskite nitrides. Phys. Rev. Mater., **4** 024408 (2020).

[34] T. Hajiri, S. Ishino, K. Matsuura, H. Asano, Electrical current switching of the noncollinear antiferromagnet Mn_3GaN, Appl. Phys. Lett., **115** 052403 (2019).

[35] T. Hajiri, K. Matsuura, K. Sonoda, E. Tanaka, K. Ueda, H. Asano, Spin-Orbit-Torque Switching of Noncollinear Antiferromagnetic Antiperovskite Manganese Nitride Mn_3GaN, Phys. Rev. Appl., **16** 024003 (2021).

[36] E. Y. Tsymbal, E. R. A. Dagotto, C.-B. Eom, R. Ramesh, Multifunctional Oxide Heterostructures (Oxford, 2012; online edn, Oxford Academic, 24 Jan. 2013), https://doi.org/10.1093/acprof:oso/9780199584123.001.0001, accessed 6 Apr. 2023.

[37] G.J.v.d. Berg, Anomalies in dilute metallic solutions of transition metals. J. G. Daunt, D. O. Edwards, F. J. Milford, M. Yaqub (eds) Low-Temperature Physics LT9, **4** 955–984 (1965).

[38] J. Kondo, Resistance Minimum in Dilute Magnetic Alloys. Prog. Theor. Phys., **32** 37-49 (1964).

[39] P.W. Anderson, Localized Magnetic States in Metals. Phys. Rev., **124** 41-53 (1961).

[40] M. Ramanzani, H.M. Sauer, A. Holz, R. Birringer, H. Gleiter, On the Kondo-effect in dilute alloys of iron and nanoscaled copper. Zeitschrift für Physik B Condensed Matter, **100** 39-45 (2014).

[41] W. J. De Haas, J. D. Boer, G. J. V. D. Berg, The electrical resistance of gold, copper and lead at low temperatures. Physica, **1** 1115-1124 (1934).

[42] H. Watanabe, M. Ogata, Crossover from dilute-Kondo system to heavy-fermion system, Phys. Rev. B, **81** 113111 (2010).

[43] F.C. Ragel, P.d.V. du Plessis, A.M. Strydom, Effects of La dilution on the $CePt_2Si_2$ Kondo lattice, J. Phys. Condens. Matter, **20** 055218 (2008).

[44] X. Ding, J. Xing, G. Li, L. Balicas, K. Gofryk, H.-H. Wen, Crossover from Kondo to Fermi-

liquid behavior induced by high magnetic field in 1T−VTe_2 single crystals, Physical Review B, **103** 125115 (2021).

[45] J. Chen, Z. Wang, S. Zheng, C. Feng, J. Dai, Z. Xu, Antiferromagnetic Kondo lattice compound $CePt_3P$, Sci. Rep., **7** 41853 (2017).

[46] A. Generalov, D.A. Sokolov, A. Chikina, Y. Kucherenko, V.N. Antonov, L.V. Bekenov, S. Patil, A.D. Huxley, J.W. Allen, K. Matho, K. Kummer, D.V. Vyalikh, C. Laubschat, Insight into the temperature dependent properties of the ferromagnetic Kondo lattice YbNiSn, Phys. Rev. B, **95** 184433 (2017).

[47] J.-H. Chen, L. Li, W. G. Cullen, E. D. Williams, M. S. Fuhrer, Tunable Kondo effect in graphene with defects, Nat. Phys., **7** 535-538 (2011).

[48] K. R. Sapkota, F. S. Maloney, W. Wang, Observations of the Kondo effect and its coexistence with ferromagnetism in a magnetically undoped metal oxide nanostructure, Phys. Rev. B, **97** 144425 (2018).

[49] S. M. Cronenwett, T. H. Oosterkamp, L. P. Kouwenhoven, A Tunable Kondo Effect in Quantum Dots. Science **281**, 540-544 (1998)

[50] R.R. Nair, I.L. Tsai, M. Sepioni, O. Lehtinen, J. Keinonen, A.V. Krasheninnikov, A.H. Castro Neto, M.I. Katsnelson, A.K. Geim, I.V. Grigorieva, Dual origin of defect magnetism in graphene and its reversible switching by molecular doping. Nat. Commun., **4** 2010 (2013).

[51] S. Seiro, L. Jiao, S. Kirchner, S. Hartmann, S. Friedemann, C. Krellner, C. Geibel, Q. Si, F. Steglich, and S. Wirth, Evolution of the Kondo lattice and non-Fermi liquid excitations in a heavy-fermion metal. Nat. Commun., **9** 3324 (2018).

[52] S. Kobayashi, Y. Yoshino, S. Tsuji, S. Masafumi, F. Iga, Kondo Effect in the Long-Range Antiferromagnetic Ordered State –$Ce_xNd_{1-x}B_6$–. J. Phys. Soc. Japan, **72** 25-28 (2003).

[53] H.H. Lai, S.E. Grefe, S. Paschen, Q. Si, Weyl-Kondo semimetal in heavy-fermion systems, Proc. Natl. Acad. Sci. U. S. A., **115** 93-97 (2018).

[54] A. Maurya, R. KulkarniA. Thamizhavel, D. Paudyal and S. K. Dhar, Kondo Lattice and An-

tiferromagnetic Behavior in Quaternary $CeTAl_4Si_2$ (T = Rh, Ir) Single Crystals, J. Phys. Soc. Japan, **85** 034720 (2016).

[55] D. K. Singh, A. Thamizhavel, J. W. Lynn, S. Dhar, J. Rodriguez-Rivera, T. Herman, , Field-induced quantum fluctuations in the heavy fermion superconductor CeCu(2)Ge(2), Sci. Rep., **1** 117 (2011).

[56] G. Zwicknagl, Kondo Effect and Antiferromagnetism in $CeCu_2Ge_2$: An Electronic Structure Study, J. Low Temp. Phys., **147** 123-134 (2007).

[57] O. Stockert, F. Steglich, Unconventional Quantum Criticality in Heavy-Fermion Compounds. Annu. Rev. Condens. Matter Phys., **2** 79-99 (2011).

[58] J. Wang, Y.-f. Yang, Nonlocal Kondo effect and quantum critical phase in heavy-fermion metals. Phys. Rev. B, **104** 165120 (2021).

[59] S. Nakatsuji, K. Kuga, Y. Machida, T. Tayama, T. Sakakibara, Y. Karaki, H. Ishimoto, S. Yonezawa, Y. Maeno, E. Pearson, G.G. Lonzarich, L. Balicas, H. Lee, Z. Fisk, Superconductivity and quantum criticality in the heavy-fermion system β-$YbAlB_4$. Nat. Phys., **4** 603-607 (2008).

[60] K. R. Shirer, A. C. Shockley, A. P. Dioguardi, J. Crocker, C. H. Lin, N. apRoberts-Warren, D. M. Nisson, P. Klavins, J. C. Cooley, Y.-f. Yang, and N. J. Curro, Proc. Natl. Acad. Sci. USA **109**, E3067 (2012).

[61] J-P. Jardin, J. Labbe, Phase transitions and band structure in metallic perovskites (carbides and nitrides), J. Solid State Chem. **46** 275-293 (1983).

[62] R. Navarro, J.A. Rojo, Spin-Glass-Like Phase in $Mn_{4-x}Ga_xN$ Solid Solution, Magnetic Properties for x = 0.75, 0.85, 0.9, 0.95 and 1.0, J. Magn. Magn. Mater., **59** 221-234 (1986).

[63] B. H. Rimmler, B. K. Hazra, B. Pal, K. Mohseni, J. M. Taylor, A. Bedoya-Pinto, H. Deniz, M. Tangi, I. Kostanovskiy, C. Luo, R. R. Neumann, A. Ernst, F. Radu, I. Mertig, H. L. Meyerheim, and S. S. P. Parkin, Atomic Displacements Enabling the Observation of the Anomalous Hall Effect in a Non-Collinear Antiferromagnet. Adv. Mater. **35**, 2209616 (2023).

[64] D. Khadka, T. R. Thapaliya, S. H. Parra, X. Han, J. Wen, R. F. Need, P. Khanal, W. Wang, J.

Zang, J. M. Kikkawa, L. Wu, S. X. Huang, Kondo physics in antiferromagnetic Weyl semimetal $Mn_{3+x}Sn_{1-x}$ films, Sci. Adv. , **6** 1-8 (2020).

[65] V. K. Anand, D. T. Adroja, A. Bhattacharyya, B. Klemke, and B. Lake, Kondo lattice heavy fermion behavior in $CeRh_2Ga_2$. J. Phys. Condens. Matter 29, 135601 (2017).

[66] K. Shi, Y. Sun, J. Yan, S. Deng, L. Wang, H. Wu, P. Hu, H. Lu, M. I. Malik, Q. Huang, C. Wang, Baromagnetic Effect in Antiperovskite $Mn_3Ga_{0.95}N_{0.94}$ by Neutron Powder Diffraction Analysis. Adv. Mater. **28**, 3761- 3767 (2016).

[67] D. Fruchart, E. F. Bertaut, J. P. Bouchaud, R. Fruchart, Diffraction Neutronique De Mn_3GaN, Solid State Commun. **6** 251-256 (1986).

[68] E. F. Bertaut, D. Fruchart, J. P. Bouchaud, R. Fruchart, DIFFRACTION NEUTRONIQUE DE Mn_3GaN. Solid State Commun. **6**, 251 (1986).

[69] Y. M. Zhao and P. F. Zhou, Metal–insulator transition in helical $SrFeO_{3-}$ antiferromagnet. J. Magn. Magn. Mater. **281**, 214 (2004).

[70] J. Fowlie, A. B. Georgescu, A. Suter, B. Mundet, C. Toulouse, N. Jaouen, M. Viret, C. Domínguez, M. Gibert, Z. Salman, T. Prokscha, D. T. L. Alexander, J. Kreisel, A. Georges, A. J. Millis, and J.-M. Triscone, Metal–insulator transition in composition-tuned nickel oxide films. J. Phys. Condens. Matter **35**, 304001 (2023).

[71] B. Gao, T. Chen, X.-C. Wu, M. Flynn, C. Duan, L. Chen, C.-L. Huang, J. Liebman, S. Li, F. Ye, M. B. Stone, A. Podlesnyak, D. L. Abernathy, D. T. Adroja, M. D. Le, Q. Huang, A. H. Nevidomskyy, E. Morosan, L. Balents, and P. Dai, Diffusive excitonic bands from frustrated triangular sublattice in a singlet-ground-state system. Nat. Commun. **14**, 2051 (2023).

[72] W.J. Feng, D. Li, Y.F. Deng, Q. Zhang, H.H. Zhang, Z.D. Zhang, Magnetic and transport properties of $Mn_{3+x}Ga_{1-x}N$ compounds, J. Mater. Sci., **45**, 2770-2774 (2010).

[73] J. R. Chelikowsky, and S. G. Louie, eds. Quantum Theory of Real Materials (Berlin: Springer Science and Business Media) **348**, 219 (1996).

[74] M. Yokoyama, S. Nakano, S. Someya, T. Nakada, N. Wada, H. Kawanaka, H. Bando, K. Tenya,

A. Kondo, and K. Kindo, Low-temperature specific heat for ferromagnetic and antiferromagnetic orders in $CaRu_{1-x}Mn_xO_3$. J. Phys. Conf. Ser. **391**, 012114 (2012).

[75] W. Niu, M. Gao, X. Wang, F. Song, J. Du, X. Wang, Y. Xu, R. Zhang, Evidence of weak localization in quantum interference effects observed in epitaxial $La_{0.7}Sr_{0.3}MnO_3$ ultrathin films, Sci Rep, **6** 26081 (2016).

[76] B. L. Al'tshuler and A. G. Aronov, Contribution to the theory of disordered metals in strongly doped semiconductors. Sov. Phys. JEPT **77**, 2028-2044 (1979).

[77] C. Li, M. Boubeche, L. Zeng, Y. Ji, Q. Li, D. Guo, Q. Zhu, D. Zhong, H. Luo, and H. Wang, Electron–Electron Interaction and Weak Antilocalization Effect in a Transition Metal Dichalcogenide Superconductor. Phys. Status Solidi - Rapid Res. Lett. **16**, 2100650 (2022).

[78] J. Joseph, C. Bansal, K. J. Reddy, and A. Rajanikanth, Electron–electron interaction dominated resistivity minimum in quasi-continuous Ag nanocluster films. AIP Adv. **10**, 125223 (2020).

[79] P. A. Lee and T. V. Ramakrishnan, Disordered electronic systems. Rev. Mod. Phys. **57**, 287 (1985).

[80] Y. Xu, J. Zhang, G. Cao, C. Jing, S. Cao, Low-temperature resistivity minimum and weak spin disorder of polycrystalline $La_{2/3}Ca_{1/3}MnO_3$ in a magnetic field, Physical Review B, **73** 224410 (2006).

[81] M. Szlawska, D. Gnida, and D. Kaczorowski, Magnetic and electrical transport behavior in the crystallographically disordered compound U_2CoSi_3 Phys. Rev. B **84**, 134410 (2011).

[82] N. Rivier and K. Adkins, Resistivity of spin glasses. J. Phys. F: Metal Phys. **5**, 1745 (1975).

[83] B. Gorshunov, A. S. Prokhorov, S. Kaiser, D. Faltermeier, S. Yasin, M. Dumm, N. Drichko, E. S. Zhukova, I. E. Spektor, and S. Vongtragool, Charge localization due to RKKY interaction in the spin-glass AuFe. Europhys. Lett. (EPL) **76**, 938 (2006).

[84] S. Ghosh, R. G. Tanguturi, P. Pramanik, D. C. Joshi, P. K. Mishra, S. Das, and S. Thota, Low-temperature anomalous spin correlations and Kondo effect in ferromagnetic $SrRuO_3/LaNiO_3/La_{0.7}Sr_{0.3}MnO_3$ trilayers. Phys. Rev. B **99**, 115135 (2019).

[85] S. Y. Li, L. Taillefer, D. G. Hawthorn, M. A. Tanatar, J. Paglione, M. Sutherland, R. W. Hill, C. H. Wang, and X. H. Chen, Giant Electron-Electron Scattering in the Fermi-Liquid State of Na$_{0.7}$CoO$_2$. Phys. Rev. Lett. **93**, 056401 (2004).

[86] C. Echevarria-Bonet, D. P. Rojas, J. I. Espeso, J. Rodriguez Fernandez, L. Rodriguez Fernandez, E. Bauer, S. Burdin, S. G. Magalhaes, and L. Fernandez Barquin, Breakdown of the coherence effects and Fermi liquid behavior in YbAl$_3$ nanoparticles. J. Phys. Condens. Matter **30**, 135604 (2018).

[87] R. L. Liboff, G. K. Schenter, Electron-phonon scattering contributions to metallic resistivity at 0 K, Phys. Rev. B, **54** 23 (1996).

[88] I. S. Sandalov and A. N. Podmarkov, Possibility of inducing the Kondo effect by a magnetic field in a ferromagnet. Sov. Phys. JETP **88**, 1321-1335 (1985).

[89] L. Kouwenhoven and L. Glazman, Revival of the Kondo effect. Phys. world **14**, 33 (2001).

[90] C.P. Lin, C.Y. Hsu, S.J. Sun, H. Chou, The Kondo effect and carrier transport in amorphous Cr-doped In$_2$O$_3$ thin films, AIP Adv., **2** 042186 (2012).

[91] E. J. Guo, L. Wang, Z. P. Wu, L. Wang, H. B. Lu, K. J. Jin, and J. Gao, Magnetic field mediated low-temperature resistivity upturn in electron-doped La$_{1-x}$Hf$_x$MnO$_3$ manganite oxidesJ. Appl. Phys. **112**, 123710 (2012).

[92] P. Saha, M. Singh, V. Nagpal, P. Das, and S. Patnaik, Scaling analysis of anomalous Hall resistivity and magnetoresistance in the quasi-two-dimensional ferromagnet Fe$_3$GeTe$_2$ Phys. Rev. B **107** 035115 (2023).

[93] J. Zhang, W.-J. Ji, J. Xu, X.-Y. Geng, J. Zhou, Z.-B. Gu, Shu-Hua Yao, and S.-T. Zhang, Giant positive magnetoresistance in half-metallic double-perovskite Sr$_2$CrWO$_6$ thin films. Sci. Adv. **3**, e1701473 (2017).

[94] V. H.-Hoang, N. K. Chung, and H. J. Kim, Electrical transport properties and Kondo effect in La$_{1-x}$Pr$_x$NiO$_{3-}$ thin films. Sci. Rep. **11**, 5391 (2021).

[95] B. Zhao, P. Cheng, H. Pan, S. Zhang, B. Wang, G. Wang, F. Xiu, and F. Song, Weak antilocalization in Cd_3As_2 thin films. Sci. Rep. **6**, 22377 (2016).

[96] H. Afzal, S. Bera, A. K. Mishra, M. Krishnan, M. M. Patidar, R. Venkatesh, and V. Ganesan, Correlation Between Magnetic Ordering and Crossover from Weak Anti-Localization (WAL) to Weak Localization (WL) in Cobalt- and Manganese-Doped $Bi_{0.94}Sb_{0.06}$ Topological Insulator Nanoparticles. J. Supercond. Nov. Magn. **33**, 1659 (2020).

[97] D. V. Baxter, R. Richter, M. L. Trudeau, R. W. Cochrane, and J. O. Strom-Olsen, Fitting to magnetoresistance under weak localization in three dimensions. J. Phys. **50**, 1673 (1989).

[98] N. Shahi, A. K. Jena, G. K. Shukla, V. Kumar, S. Rastogi, K. K. Dubey, I. Rajput, S. Baral, A. Lakhani, S.-C. Lee, S. Bhattacharjee, and S. Singh, Antisite disorder and Berry curvature driven anomalous Hall effect in the spin gapless semiconducting Mn_2CoAl Heusler compound. Phys. Rev. B **106**, 245137 (2022).

[99] S. Malick, A. Ghosh, C. K. Barman, A. Alam, Z. Hossain, P. Mandal, and J. Nayak, Weak antilocalization effect and triply degenerate state in Cu-doped CaAuAs. Phys. Rev. B **105**, 165105 (2022).

[100] A. Kawabata, Theory of Negative Magnetoresistance I. Application to Heavily Doped Semiconductors. J. Phys. Soc. Jpn. **49**, 628-637 (1980).

[101] S. Barua, M. C. Hatnean, M. R. Lees, G. Balakrishnan, Signatures of the Kondo effect in VSe2, Sci. Rep., **7** 10964 (2017).

[102] Y. Katayama, S. Tanaka, Resistance Anomaly and Negative Magnetoresistance in n-Type InSb at Very Low Temperatures, Phys. Rev., **153** 873-882 (1967).

[103] T. Sekitani, M. Naito, and N. Miura, Kondo effect in underdoped n-type superconductors. Phys. Rev. B **67**, 174503 (2003).

[104] T.A. Costi, L. Bergqvist, A. Weichselbaum, J. von Delft, T. Micklitz, A. Rosch, P. Mavropoulos, P.H. Dederichs, F. Mallet, L. Saminadayar, C. Bauerle, Kondo decoherence: finding the right spin model for iron impurities in gold and silver, Phys. Rev. Lett., **102** 056802 (2009).

[105] D. G.-Gordon, J. Göres, M. A. Kastner, H. Shtrikman, D. Mahalu, and U. Meirav, From the Kondo Regime to the Mixed-Valence Regime in a Single-Electron Transistor, Phys. Rev. Lett., **81**, 5225 (1998).

[106] D.C. Langreth, Friedel Sum Rule for Anderson's Model of Localized Impurity States, Phys. Rev., **150** 516-518 (1966).

[107] A. A. Zvyagin, P. Schlottmann, Finite-size effects in a metallic multichannel ring with Kondo impurity Persistent currents and magnetoresistance, Phys. Rev. B, **54** 15191 (1996).

[108] A. M. Tsveliek, P.B. Wiegmann, Exact Solution of the Multichannel Kondo Problem, Scaling, and Integrability. J. Stat. Phys., **38** 125-147 (1985).

[109] C. M. Hurd, The Hall Effect in Metals and Alloys (Plenum, New York, 1972).

[110] K. Manna, L. Muechler, T. H. Kao, R. Stinshoff, Y. Zhang, J. Gooth, N. Kumar, G. Kreiner, K. Koepernik, and R. Car, J. Kübler, G. H. Fecher, C. Shekhar, Y. Sun, and C. Felser, From Colossal to Zero: Controlling the Anomalous Hall Effect in Magnetic Heusler Compounds via Berry Curvature Design. Phys. Rev. X **8**, 041045 (2018).

[111] A. M. Vibhakar, D. D. Khalyavin, P. Manuel, J. Liu, A. A. Belik, and R. D. Johnson, Spontaneous Rotation of Ferrimagnetism Driven by Antiferromagnetic Spin Canting. Phys. Rev. Lett. **124**, 127201 (2020).

[112] I. Samathrakis, H. Zhang, Tailoring the anomalous Hall effect in the noncollinear antiperovskite Mn 3 GaN. Phys. Rev. B **101**, 214423 (2020).

[113] K. Momma and F. Izumi, "VESTA 3 for three-dimensional visualization of crystal, volumetric and morphology data", J. Appl. Crystallogr. **44**, 1272-1276 (2011).

[114] A. Ghods, C. Zhou, and I. T. Ferguson, Structural and optical properties of (Zn,Mn)O thin films prepared by atomic layer deposition, J. Vac. Sci. Technol. A **38**, 042408 (2020).

[115] C. I. M. Rodríguez, M. Á. L. Álvarez, J. d. J. F. Rivera, G. G. C. Arízaga, and Carlos R. Michel, α-Ga2O3 as a Photocatalyst in the Degradation of Malachite Green, ECS J. Solid State Sci. Technol., **8** (7) Q3180-Q3186 (2019).

[116] D. Shah, S. Bahr, P. Dietrich, M. Meyer, A. Thißen, M. R. Linford, Nitrogen gas (N_2), by near-ambient pressure XPS, Surf. Sci. Spectra **26**, 014023 (2019).

[117] X. Zhang, Q. Yuan, T. Gao, Y. Ren, H. Wu, Q. Huang, J. Zhao, X. Wang, Y. Yuan, C. Xu, Y. Hu, J.J. Dynes, J. Zhou, S. Zhou, Y. Liu, B. Song, Transition from antiferromagnetic ground state to robust ferrimagnetic order with Curie temperatures above 420 K in manganese-based antiperovskite-type structures, J. Mater. Chem. C, **6** 13336-13344 (2018).

[118] R. Niewa, Z. Hu, C. Grazioli, U. Róßler, M.S. Golden, M. Knupfer, J. Fink, H. Giefers, G. Wortmann, F.M.F. e Groot, and F.J. DiSalvo, XAS spectra of Ce_2[MnN3] at the Ce-M4,5, Ce-L3, Mn-L2,3 and N-K thresholds, J. Alloys Compd **346** 129-133 (2002).

[119] C. W. Pao, P. D. Babu, H. M. Tsai, J. W. Chiou, S. C. Ray, S. C. Yang, F. Z. Chien, W. F. Pong, M.-H. Tsai, C. W. Hsu, L. C. Chen, C. C. Chen, K. H. Chen, H.-J. Lin, J. F. Lee, J. H. Guo, Electronic structures of group-III–nitride nanorods studied by x-ray absorption, x-ray emission, and Raman spectroscopy, Appl. Phys. Lett. **88**, 223113 (2006).